Cell Metabolism

Article

Adhesion-mediated mechanosignaling forces mitohormesis

Graphical abstract

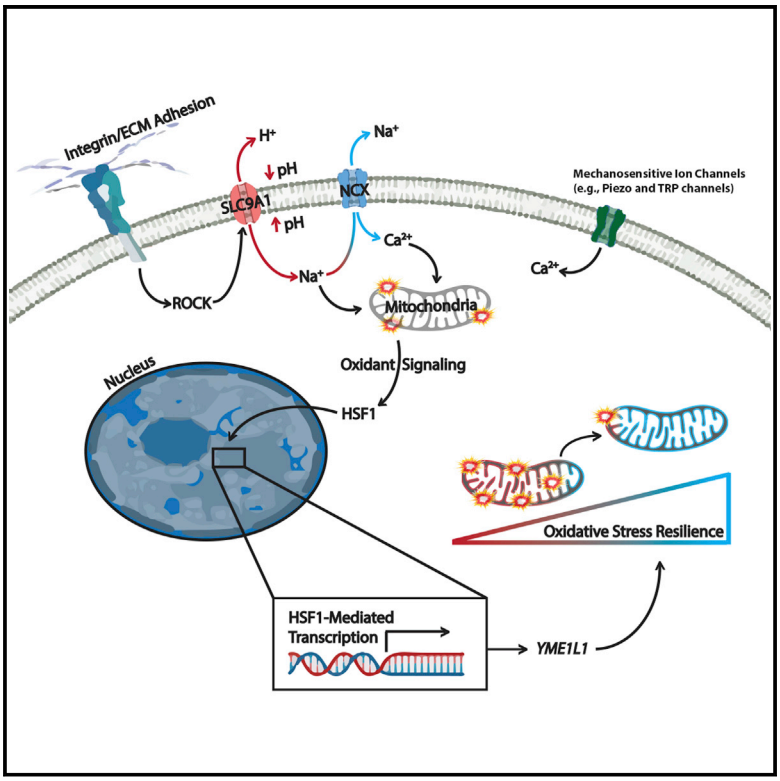

Highlights

- Cell-ECM mechanosignaling influences mitochondrial structure and function
- Cellular mechanosignaling activates an HSF1-mediated stress response
- Stiff ECM alters redox homeostasis and metabolism via mitochondrial reprogramming
- Stiff microenvironments confer redox stress resilience to cells via HSF1 and YME1L1

Authors

Kevin M. Tharp, Ryo Higuchi-Sanabria, Greg A. Timblin, ..., Danielle L. Swaney, Andrew Dillin, Valerie M. Weaver

Correspondence

valerie.weaver@ucsf.edu

In brief

Tharp et al. demonstrate that adhesion-mediated mechanosignaling dictates cellular metabolic programing. Mechanosensitive ion exchange and an HSF1-mediated mitochondrial stress response alters metabolic programing of cells actively adapting to mechanically distinct microenvironments. These findings offer one explanation for metabolic phenotypes observed in some epithelial cells residing within fibrotic/stiffened tumor tissue microenvironments.

Tharp et al., 2021, Cell Metabolism *33*, 1–20
June 1, 2021 Published by Elsevier Inc.
https://doi.org/10.1016/j.cmet.2021.04.017

CellPress

Please cite this article in press as: Tharp et al., Adhesion-mediated mechanosignaling forces mitohormesis, Cell Metabolism (2021), https://doi.org/10.1016/j.cmet.2021.04.017

Cell Metabolism

CellPress

Article

Adhesion-mediated mechanosignaling forces mitohormesis

Kevin M. Tharp,[1] Ryo Higuchi-Sanabria,[2] Greg A. Timblin,[3] Breanna Ford,[4,5] Carlos Garzon-Coral,[6] Catherine Schneider,[5] Jonathon M. Muncie,[1] Connor Stashko,[1] Joseph R. Daniele,[7] Andrew S. Moore,[8] Phillip A. Frankino,[2] Stefan Homentcovschi,[2] Sagar S. Manoli,[9] Hao Shao,[10] Alicia L. Richards,[11] Kuei-Ho Chen,[11] Johanna ten Hoeve,[12] Gregory M. Ku,[13] Marc Hellerstein,[5] Daniel K. Nomura,[4,5] Karou Saijo,[3] Jason Gestwicki,[10] Alexander R. Dunn,[4] Nevan J. Krogan,[11] Danielle L. Swaney,[11] Andrew Dillin,[2] and Valerie M. Weaver[1,14,15,*]

[1]Center for Bioengineering and Tissue Regeneration, Department of Surgery, University of California, San Francisco, San Francisco, CA 94143, USA

[2]Department of Molecular & Cellular Biology, Howard Hughes Medical Institute, University of California Berkeley, Berkeley, CA 94597, USA

[3]Department of Molecular and Cell Biology, University of California Berkeley, Berkeley, CA 94720, USA

[4]Department of Nutritional Sciences and Toxicology, University of California Berkeley, Berkeley, CA 94720, USA

[5]Novartis, Berkeley Center for Proteomics and Chemistry Technologies and Department of Chemistry, University of California Berkeley, Berkeley, CA 94720, USA

[6]Chemical Engineering Department, Stanford University, Stanford, CA 94305, USA

[7]MD Anderson Cancer Center, South Campus Research, Houston, CA 77054, USA

[8]Janelia Research Campus, Howard Hughes Medical Institute, Ashburn, VA 20147, USA

[9]Department of Cell and Tissue Biology, University of California, San Francisco, San Francisco, CA 94143, USA

[10]Department of Pharmaceutical Chemistry, University of California, San Francisco, San Francisco, CA 94158, USA

[11]Quantitative Biosciences Institute (QBI), J. David Gladstone Institutes, Department of Cellular and Molecular Pharmacology, University of California, San Francisco, San Francisco, CA 94158, USA

[12]UCLA Metabolomics Center, Department of Molecular and Medical Pharmacology, University of California, Los Angeles, Los Angeles, CA 90095, USA

[13]Diabetes Center, Division of Endocrinology and Metabolism, Department of Medicine, UCSF, San Francisco, CA 94143, USA

[14]Department of Bioengineering and Therapeutic Sciences and Department of Radiation Oncology, Eli and Edythe Broad Center of Regeneration Medicine and Stem Cell Research, and The Helen Diller Family Comprehensive Cancer Center, University of California, San Francisco, San Francisco, CA 94143, USA

[15]Lead contact

*Correspondence: valerie.weaver@ucsf.edu

https://doi.org/10.1016/j.cmet.2021.04.017

SUMMARY

Mitochondria control eukaryotic cell fate by producing the energy needed to support life and the signals required to execute programed cell death. The biochemical milieu is known to affect mitochondrial function and contribute to the dysfunctional mitochondrial phenotypes implicated in cancer and the morbidities of aging. However, the physical characteristics of the extracellular matrix are also altered in cancerous and aging tissues. Here, we demonstrate that cells sense the physical properties of the extracellular matrix and activate a mitochondrial stress response that adaptively tunes mitochondrial function via solute carrier family 9 member A1-dependent ion exchange and heat shock factor 1-dependent transcription. Overall, our data indicate that adhesion-mediated mechanosignaling may play an unappreciated role in the altered mitochondrial functions observed in aging and cancer.

INTRODUCTION

Alterations in mitochondrial function permit cancer cells to rapidly proliferate and metastasize and aging cells to regulate senescence phenotypes induced by DNA damage. Mitochondria provide a privileged metabolic compartment where oxidative phosphorylation (OxPhos) consumes oxygen and reducing equivalents to produce ATP. While OxPhos provides an efficient means to produce ATP, it can create collateral cellular damage through the release of reactive oxygen species (ROS), which can oxidize proteins, lipids, and nucleic acids. In response to elevated mitochondrial ROS exposure, cancer and aging cells activate adaptive stress responses that allow them to harness ROS-mediated proliferation and migration effects without activating ROS-mediated cell death (Balaban et al., 2005; Reczek and Chandel, 2017; Scialò et al., 2016; Wallace, 2012). These types of oxidative stress resilience (OxSR) programs alter cellular metabolism to enhance ROS buffering in the cytosol to limit damage caused by mitochondrial ROS.

Please cite this article in press as: Tharp et al., Adhesion-mediated mechanosignaling forces mitohormesis, Cell Metabolism (2021), https://doi.org/10.1016/j.cmet.2021.04.017

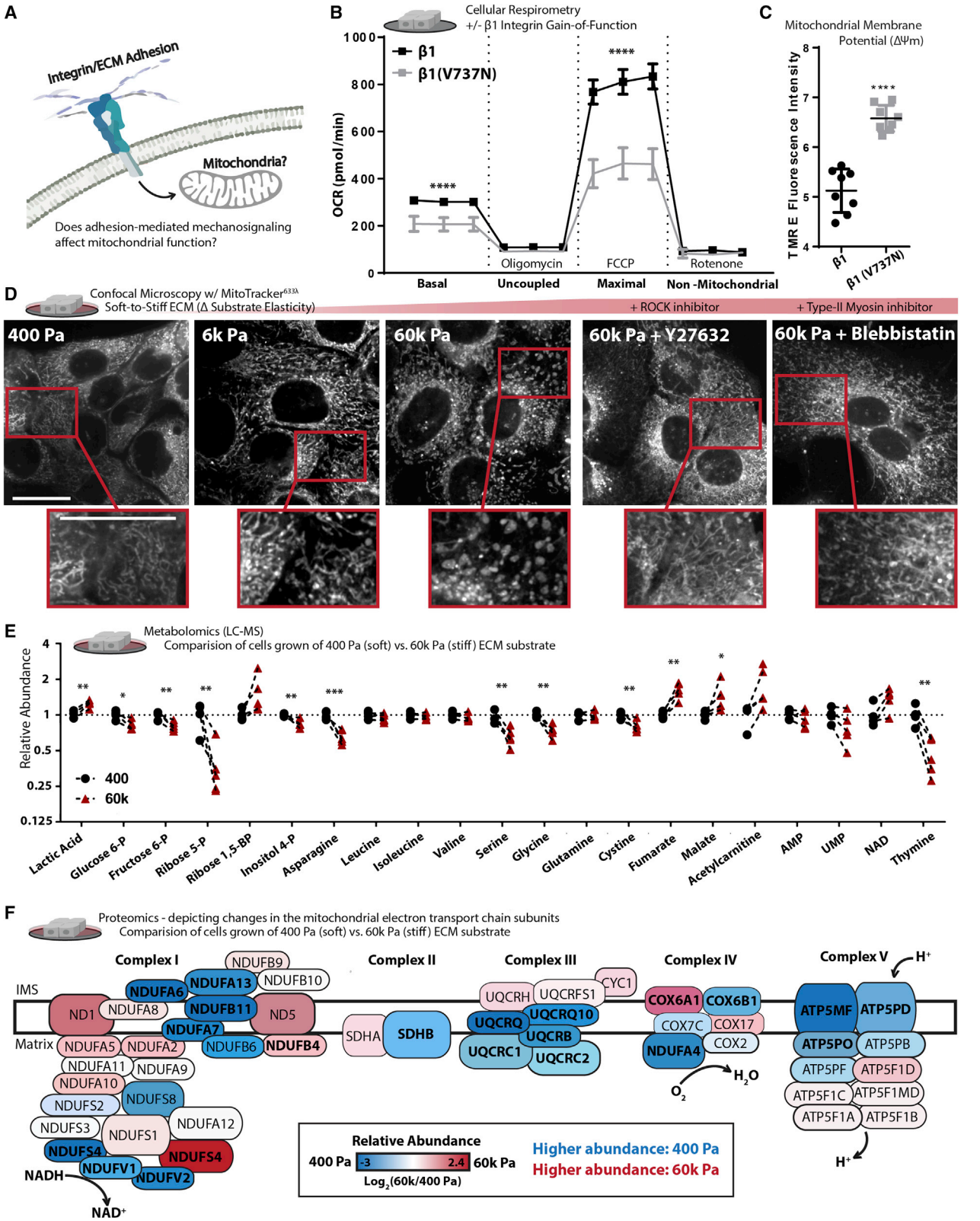

(legend on next page)

Please cite this article in press as: Tharp et al., Adhesion-mediated mechanosignaling forces mitohormesis, Cell Metabolism (2021), https://doi.org/10.1016/j.cmet.2021.04.017

The overproduction of ROS via mitochondrial dysfunction is thought to occur because of the biochemical composition of the aged or tumor microenvironment (TME) (Fane and Weeraratna, 2020; Ladiges et al., 2010; Sun et al., 2016; Vyas et al., 2016). However, the physical characteristics of the cellular microenvironment are also altered by cancer and aging—and can affect cell fate, function, and metabolism by regulating the activity of stress- and ROS-associated transcription factors (Fane and Weeraratna, 2020; Miroshnikova et al., 2016; Northcott et al., 2018; Oudin and Weaver, 2016). Sensing the mechanical properties of the extracellular matrix (ECM) can also affect cellular metabolism by regulating the levels and/or activity of cytoplasmic enzymes responsive to mechanosignaling-induced cytoskeletal dynamics (Papalazarou et al., 2020; Park et al., 2020). Cellular mechanosignaling relies on adhesion receptors, such as integrins, transducing signals that mechanically entrain the cytoskeleton to the ECM, and these cytoskeletal remodeling events can affect the topological distribution of metabolic organelles, cargoes, and enzymes (Anesti and Scorrano, 2006; Northcott et al., 2018; Schedin and Keely, 2011). Cytoskeletal dynamics also play a critical role in the regulation of mitochondrial structure (Helle et al., 2017; Manor et al., 2015; Moore et al., 2016), and mechanosensitive transcription factors can alter mitochondrial gene expression (Tharp et al., 2018). Because mitochondrial structure influences mitochondrial function, we sought to determine whether and how adhesion-mediated mechanosignaling affects mitochondrial function (Figure 1A).

RESULTS

Mechanosignaling alters mitochondrial structure and function

We investigated the relationship between adhesion-dependent mechanosignaling and mitochondrial function by exogenously expressing a β1-integrin "gain-of-function" mechanosignaling model in nonmalignant human mammary epithelial cells (MECs; MCF10A). Expression of the β1-integrin (V737N, point mutation) promotes focal adhesion assembly, phosphorylation of focal adhesion kinase (FAK) (Figure S1A), cytoskeletal remodeling, actomyosin tension (Paszek et al., 2005), and the suppression of mitochondrial oxygen consumption (Figure 1B). Cellular respiration is primarily a product of OxPhos, in which the mitochondrial electron transport chain (ETC) consumes oxygen and reducing equivalents to produce ATP. Contrary to the paradigm that suppressed mitochondrial function (e.g., reduced respiration) occurs owing to the loss of the mitochondrial membrane potential ($\Delta\Psi m$), the β1(V737N)-integrin-expressing MECs had higher, not lower, mitochondrial membrane potential (Figure 1C). To ensure that these phenotypes were not due to an indirect effect of β1(V737N)-integrin expression, we varied the surface density coating of fibronectin, an ECM component and integrin adhesion ligand that increases mechanosignaling via β1-integrin (Oria et al., 2017). MECs plated on a higher density of a fibronectin surface coating (60 μM/cm^2) also showed repression of mitochondrial oxygen consumption, similar to β1(V737N)-integrin expression (Figure S1B). Furthermore, activating integrin mechanosignaling with acute exposure to manganese (Mn^{2+}) (Lin et al., 2013) suppressed mitochondrial oxygen consumption (Figure S1C). The data indicate that increased integrin mechanosignaling impacts mitochondrial function.

Integrin mechanosignaling is highly sensitive to the stiffness of the adhesion substrate, which affects mitochondrial respiration (oxygen consumption). Accordingly, we examined the mitochondrial morphology of MECs cultured for 24 h on fibronectin-coated (6 μM/cm^2) polyacrylamide hydrogel surfaces ranging in elasticity (stiffness) between normal breast (400 Pa) and tumor (6–60k Pa) ECM (Caliari and Burdick, 2016; Tharp and Weaver, 2018) (note: tissue culture polystyrene elasticity is supraphysiological, ~3G Pa). MECs cultured on this range of biologically relevant ECM elasticities displayed a variety of mitochondrial morphologies, ranging from thin interconnected filaments (400 Pa), to thickened filaments (6k Pa), and then ~300-nM diameter fragments with toroidal shapes (60k Pa) (Figures 1D, S1D, and S1E). Cells respond to ECM stiffness by ligating ECM adhesion receptors that induce Rho-GTPase and Rho-associated protein kinase (ROCK) cytoskeletal remodeling and increase actomyosin tension via type-II myosins (Butcher et al., 2009). We therefore bypassed the adhesion receptor ligation step and induced downstream mechanosignaling via an inducible ROCK, ROCK::ER (Croft and Olson, 2006), which was sufficient to suppress mitochondrial oxygen consumption (Figures S1F and S1A). In contrast, pharmacological inhibition of ROCK with Y27632 or type-II myosins with blebbistatin reduced the prevalence of the thick or toroidal mitochondrial fragments in MECs plated on the stiff ECM (Figure 1D) and restored mitochondrial oxygen consumption in the ROCK::ER cells (Figure S1G). Finally, β1(V737N)-integrin-expressing cells displayed a fragmented/toroidal mitochondrial morphology, even on the soft ECM (Figure S1H) in direct contrast to MECs expressing a wild-type β1 integrin. The data indicate that mitochondrial structure and function is sensitive to the stiffness of the ECM through integrin- and ROCK-mediated mechanosignaling.

Figure 1. Adhesion-mediated mechanosignaling alters mitochondrial structure and function of human mammary epithelial cells (MECs)

(A) Graphical representation of the experimental question.

(B) Mitochondrial oxygen consumption rate (OCR) of β1-integrin or β1(V7373N)-expressing MECs (100k cells per well, n = 5 wells, 3 replicate measures, repeated 3 times). Mitochondrial stress test conditions: uncoupled, 1 μM oligomycin; maximal, 1 μM trifluoromethoxy carbonylcyanide phenylhydrazone (FCCP); non-mitochondrial, 1 μM antimycin A and 1 μM rotenone.

(C) Mitochondrial membrane potential, measured after 1 h treatment of 10 nM tetramethylrhodamine ethyl-ester (TMRE) (n = 2 wells, repeated 4 times).

(D) Confocal microscopy depicting mitochondrial network structure in PFA-fixed cells cultured on varied soft-to-stiff fibronectin-coated (6 μM/cm^2) polyacrylamide hydrogels (soft-to-stiff ECM), for 24 h ± 10 μM Y27632 or 10 μM blebbistatin, stained with 100 nM MitoTracker (deep red FM). Scale bar, 10 μm. MitoMAPR quantification: 400 (18), 6k (20), 60k (7), 60k + Y27632 (15), and 60k + blebbistatin (12) junctions per network.

(E) Selection of metabolites measured with LC-MS from MECs cultured on soft or stiff ECM for 24 h; fold change relative to 400 Pa (n = 4–5 biological replicates; LC-MS run together, repeated 2 times).

(F) Relative abundance (fold change) of mitochondrial ETC subunits measured via timsTOF LC-MS of MECs cultured on soft or stiff ECM for 24 h (n = 3 biological replicates). Bolded text indicates *$p \leq 0.05$; locations and sizes of ETC subunits graphically depicted are approximate and not to molecular scale.

Please cite this article in press as: Tharp et al., Adhesion-mediated mechanosignaling forces mitohormesis, Cell Metabolism (2021), https://doi.org/10.1016/j.cmet.2021.04.017

Mitochondrial function affects many aspects of cellular metabolism; therefore, we broadly examined the steady-state levels of polar metabolites present in MECs cultured on ECM surfaces that mimic the soft normal ECM (400 Pa) or stiff tumor ECM (60k Pa) (Figure 1E; Videos S1, S2, and S3). MECs cultured on the stiff ECM possessed higher levels of lactate and lower levels of upstream glycolytic or pentose phosphate pathway (PPP) intermediates, which may indicate increased flux through those pathways. We also noted lower levels of serine (Chung et al. 2018) and increased levels of tricarboxylic acid (TCA) cycle intermediates such as malate and fumarate, an oncometabolite (Sciacovelli et al., 2016), which could indicate that TCA cycle flux has reduced. Indeed, previous studies have indicated that TCA cycle impairment can affect mitochondrial structure (Barasa et al., 1973). Since TCA cycle flux is largely dependent on the activity of the ETC, we mapped the compositional changes in ETC subunit abundance with mass-spectrometry-based proteomics (Figure 1F). We found that a number of critical ETC subunits changed in abundance due to ECM stiffness and their relative levels can alter properties of mitochondrial function (Jimenez-Blasco et al., 2020). These mechanosignaling-induced compositional changes in the ETC could explain the reduction of mitochondrial oxygen consumption, and the increased $\Delta\Psi m$ observed when integrin mechanosignaling is high due to decreased entry of electrons via NADH (complex I) and proton flow from the inner membrane space (IMS) into the mitochondrial matrix (MM) through ATP synthase (complex V).

Hyperglycemia and stiff ECM facilitate similar mitochondrial responses

Hyperglycemia (>5 mM glucose) is a biochemical stress that induces mitochondrial fragmentation, raises intracellular pH (pH_i) (Lindström and Sehlin, 1984), lowers extracellular pH (pH_e), and increases mitochondrial membrane potential in cultured cells (Wang et al., 2017). To explore whether the fragmented/toroidal mitochondrial morphologies induced by high cytoskeletal tension were similar to those induced by hyperglycemia, we increased the media glucose concentration from 5 mM (“low glucose”) to 25 mM (“high glucose”) for MECs plated on the soft ECM (400 Pa) and examined changes in mitochondrial organization. Lattice light sheet microscopy (LLSM), which permits live cell imaging with limited phototoxicity (Chen et al., 2014), revealed that exposing MECs to hyperglycemia induced a rapid transition of mitochondrial morphology from a filamentous network into fragmented/toroidal structures (Figure S1I; Video S4), comparable with MECs cultured on stiff ECM (Figures 1D and S1D). Moreover, cells exposed to hyperglycemia or plated on stiff ECM express similar gene profiles that have been implicated in the mitochondrial unfolded protein response (UPR^{mt}) (Aldridge et al., 2007; Lin and Haynes, 2016) (Figure S1J). Since both hyperglycemia and stiff ECM induce these mitochondrial stress response genes, we hypothesized that the reorganization of the mitochondria may reflect a pro-survival stress response (Sprenger and Langer, 2019; Youle and van der Bliek, 2012).

Because ECM stiffness induces mitochondrial reorganization by inducing cytoskeletal tension (Figure 1D) and the similarities between hyperglycemia and ECM stiffness induced mechanosignaling, we asked if hyperglycemia was sufficient to increase cellular elasticity. Atomic force microscopy (AFM) indentation revealed that hyperglycemia significantly enhanced cortical tension in MECs (Figure S1K). These findings were confirmed in a second cell line, the MDA-MB-231 MECs, which is a model of triple-negative human breast cancer. Finally, similar to the reduced respiration rate induced by manipulating cytoskeletal tension, hyperglycemia also reduced mitochondrial oxygen consumption (Figure S1L). These findings demonstrate that biochemical and physical cues appear to stimulate similar changes in mitochondrial structure and function, and these changes may occur through the same stress response.

Mitochondrial fragmentation is thought to coordinate with mitophagy (autophagosome-mediated degradation of mitochondria) to repair dysfunctional mitochondria that have reduced mitochondrial membrane potential or increased ROS production/leak (Liu and Hajnóczky, 2011; Miyazono et al., 2018; Twig and Shirihai, 2011). However, our data indicated that the mitochondrial fragmentation induced by stiff ECM had elevated mitochondrial membrane potential (Figures 2A and 2B). Thus, we reasoned that large mitochondrial fragments with toroidal morphologies likely arise through a different mechanism than has been previously described. Mitochondrial membrane potential reflects a pH differential between the mitochondrial IMS and the MM, but its measurement with lipophilic cations (TMRE) can be sensitive to changes in intracellular pH (pH_i) (Perry et al., 2011). Since we found higher levels of lactate in the MECs cultured on stiff ECM, we were concerned that these cells may have a transiently lower pH_i, which could influence the mitochondrial localization of TMRE. To verify that pH_i was not confounding our measurement of $\Delta\Psi m$, we measured pH_i of MECs cultured on the stiff ECM or exposed to hyperglycemia and found that both stresses increased pH_i (Figure 2C). One possible explanation for the mechanosensitive elevation of pH_i despite elevated glycolytic metabolism could be that ROCK, a key mechanosignaling kinase, regulates the activity of SLC9A1 (Na^+/H^+ exchanger 1 [NHE1]). SLC9A1 is responsible for the efflux of H^+ from the cytoplasm necessary for regulating the pH of the adhesion-proximal cytosol to facilitate pH-dependent conformational changes in FAK critical for its phosphorylation and mechanosignaling downstream of integrin adhesions (Choi et al., 2013; Tominaga and Barber, 1998).

SLC9A1-mediated ion exchange affects mitochondrial structure and function

To test if the elevated pH_i was responsible for the altered mitochondrial morphology observed in MECs cultured on stiff ECM, we lowered pH_i by inhibiting SLC9A1 with BIX and EIPA, and SLC4A7 (Na^+/HCO^{3-} cotransporter) with S0859. While all of these interventions lowered pHi in MECs on stiff ECM to levels equivalent or lower than soft ECM, only SLC9A1 inhibition restored the filamentous mitochondrial morphology (Figures 2D and S2A). These data suggest that a pH_i-independent effect of SLC9A1 may be responsible for the mitochondrial morphology induced by stiff ECM. SLC9A1 inhibition also restored the concentrations of approximately 60% of the significantly altered polar metabolites we measured in MECs plated on the stiff ECM back to the concentrations observed in MECs on soft ECM (Figure 2E). SLC9A1 inhibition also rescued the impaired mitochondrial oxygen consumption caused by β1(V737N)-integrin or

Please cite this article in press as: Tharp et al., Adhesion-mediated mechanosignaling forces mitohormesis, Cell Metabolism (2021), https://doi.org/10.1016/j.cmet.2021.04.017

CellPress

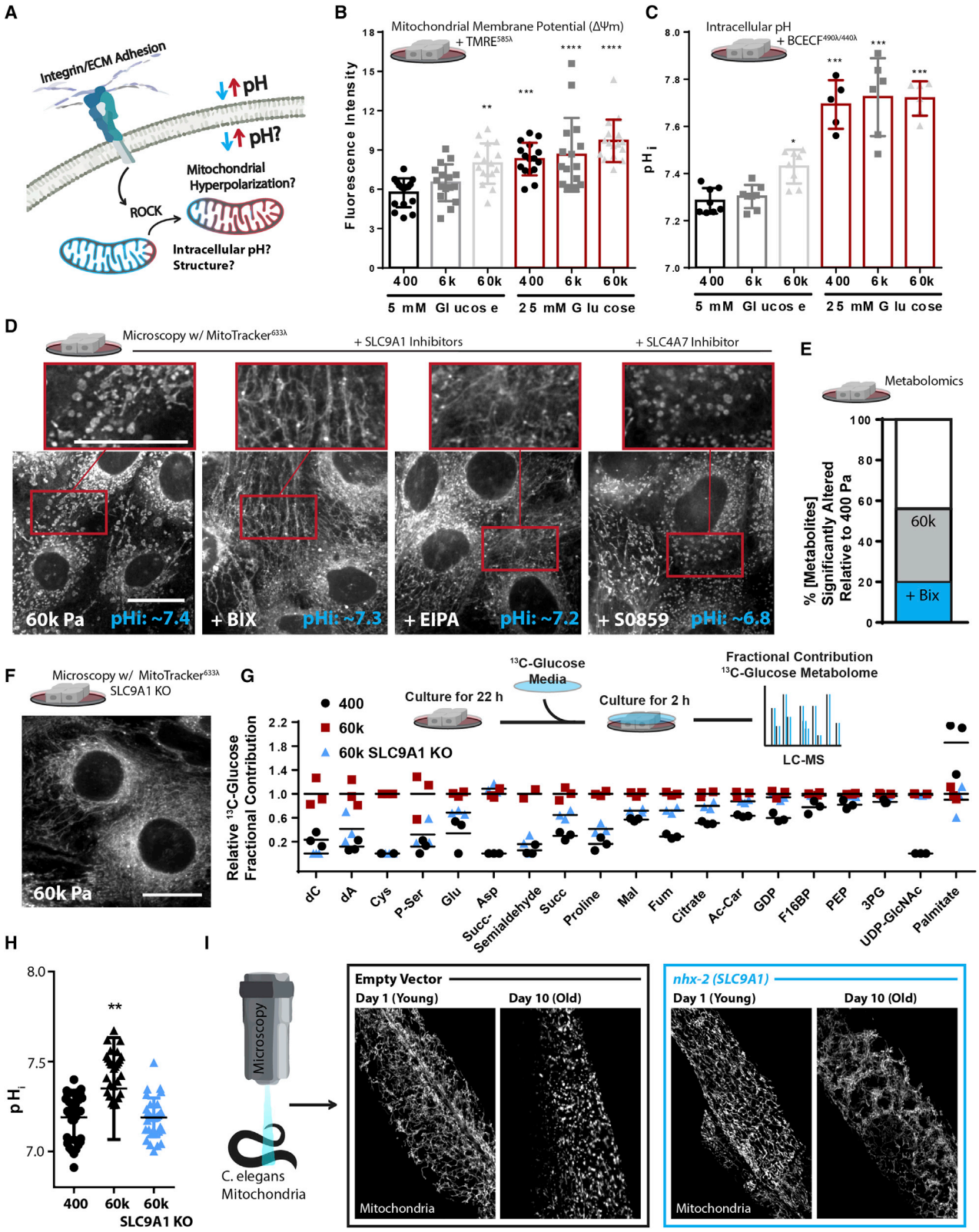

(legend on next page)

Please cite this article in press as: Tharp et al., Adhesion-mediated mechanosignaling forces mitohormesis, Cell Metabolism (2021), https://doi.org/10.1016/j.cmet.2021.04.017

ROCK::ER expression (Figures S2B–S2D). Since both hyperglycemia and ROCK activity have been shown to increase pH_i (Lindström and Sehlin, 1984; Tominaga et al., 1998), we assayed whether the proportional decrease in pH_e occurred (extracellular acidification, H^+ pumped out of the cell) and found that the pH_i:-pHe dynamics induced by hyperglycemia were sensitive to inhibition ROCK or SLC9A1 (Figure S2E).

CRISPR-mediated knockout of SLC9A1 in MECs (SLC9A1 KO) resulted in MECs that maintained a filamentous mitochondrial morphology on stiff ECM (Figures 2G and S2F). SLC9A1 KO was sufficient to normalize mitochondrial respiration in MECs exposed to hyperglycemia, as well as those on high-density fibronectin coating (Figures S2G and S2H). SCL9A1 KO cells cultured on stiff ECM metabolized glucose similarly to wild-type (WT) cells cultured on soft ECM (Figure 2G) and did not increase pH_i when cultured on stiff ECM (Figure 2H). To explore the physiological relevance of these findings, we examined the ability of *SLC9A1* to affect mitochondrial morphology in *C. elegans*, a model organism that is amenable to live microscopy of mitochondria and genetic manipulations (Nehrke and Melvin, 2002) that has been used extensively to study OxSR (Ristow and Schmeisser, 2011). RNAi-mediated knockdown of *nhx-2* (*SLC9A1* ortholog) prevented the mitochondrial fragmentation/toroidal phenotype typically found in the aged gut epithelium of this organism (Figure 2I) and instead promoted an abundant and hyperfused mitochondrial network (Figures S2I–S2L).

As a byproduct of H^+ efflux (raising pH_i, lowering pH_e) SLC9A1 facilitates Na^+ import that subsequently reverses the directionality of the Na^+/Ca^{2+} exchangers (NCX, SLC8A1-3), a process which ultimately causes mitochondrial ROS production *via* mitochondrial calcium (Ca^{2+}) overload (Brookes et al., 2004; Giorgi et al., 2018). Additionally, cellular Na^+ can affect the solubility of mitochondrial calcium phosphate precipitates, fluidity of the mitochondrial inner membrane, and ROS production from Complex III of the ETC (Hernansanz-Agustín et al., 2020). To determine whether adhesion-dependent cytoskeletal tension regulates mitochondrial Ca^{2+} content through SLC9A1 activity, we measured mitochondrial and total cellular Ca^{2+} levels in MECs plated on a range of soft-to-stiff ECM. Imaging of Rhod2-AM, calcium green-1 AM, and Fura 2 AM revealed that mitochondrial Ca^{2+} concentration was highest on the stiff ECM and could be reduced either by inhibiting or knocking out *SLC9A1* (Figures 3B and S3A). SLC9A1 inhibition was also able to suppress the mitochondrial ROS production induced by mitochondrial Ca^{2+} loading in the CGP37157 (7-Chloro-5-(2-chlorophenyl)-1,5-dihydro-4,1-benzothiazepin-2(3H)-one)-treated cells (Figures 3C, S3B, and S3C).

Increased fibronectin surface density (Figures S3D–S3F), hyperglycemia (Figure S3G), and Mn^{2+} treatment altered mitochondrial structure, increased mitochondrial Ca^{2+}, and enhanced mitochondrial ROS production, in part through the activity of SLC9A1 (Figures S3H and S3I). Consistently, treating cells with CGP37157 or kaempferol (mitochondrial calcium uniporter [MCU] activator) to increase mitochondrial Ca^{2+} content was sufficient to induce the fragmented/toroidal mitochondrial morphology in MECs plated on the soft ECM (Figure S3J). Suppression of mitochondrial ROS with 2-(2,2,6,6-tetramethylpiperidin-1-oxyl-4-ylamino)-2-oxoethyl)-triphenylphosphonium chloride (MitoTEMPO), or suppression of the mitochondrial Ca^{2+} loading via selective inhibition of the reverse mode of NCX exchangers with SN-6 (ethyl 2-[[4-[(4-nitrophenyl)methoxy]phenyl]methyl]-1,3-thiazolidine-4-carboxylate), and the MCU, with ru360 (oxo-bridged dinuclear ruthenium ammine), was also sufficient to prevent the fragment/toroid formation on stiff ECM (Figures 3D and S3K; Videos S5 and S6), providing additional evidence that Ca^{2+} overload and ROS were causative of mitochondrial remodeling.

To directly test whether ECM stiffness could impact ROS production, we next monitored the ROS production in MECs on a range of soft-to-stiff ECM over the course of 24 h (Chung et al. 2018). As expected, we found that cells seeded on stiff ECM produced more ROS than those on soft ECM, in an SLC9A1-dependent fashion (Figures 3E and S3L). Additionally, ROS production in ROCK:ER cells was also suppressed by SLC9A1 inhibition (Figure S3M). Finally, to determine whether the functional role of SLC9A1 on ROS-mediated oxidative stress was conserved in a whole organism, we tested its impact on oxidative stress in *C. elegans*. Using an reporter for oxidative stress (*gst-4p::gfp*), we found that *nhx-2* (*SLC9A1*) knockdown reduced the expression of the reporter, indicating a lower basal level of ROS production/response in these animals (Figures 3F and 3G). In agreement with the free radical theory of aging, which postulates that lifespan is shortened due to accumulated oxidation-mediated damage, we found that the lifespan of the

Figure 2. SLC9A1 facilitates stiff-ECM-induced mitochondrial programing

(A) Graphical representation of the experimental question.

(B) Mitochondrial membrane potential, measured after 1 h treatment of 10 nM tetramethylrhodamine ethyl-ester (TMRE) (n = 4 replicates, repeated 4 times, shown together).

(C) Intracellular pH (pHi) of cells grown on soft-to-stiff ECM ± 25 mM glucose, measured via 1 μM 2',7'-bis-(2-carboxyethyl)-5-(and-6)-carboxyfluorescein, acetoxymethyl ester (BCECF) (n = 2 replicates, repeated 3 to 4 times, shown together).

(D) Confocal microscopy depicting mitochondrial network structure and caption depicting pHi measurements (mean of n = 5) in MECs on 60k Pa surfaces treated with 500 nM BIX, 10 μM EIPA, 50 μM S0859, or vehicle for 24 h; 100 nM MitoTracker (deep red FM) and 1 μM BCECF (n = 2 replicates, repeated 3 times). Scale bar, 10 μm. MitoMAPR quantification: 60k (9), BIX (20), EIPA (20), and S0859 (7) junctions per network.

(E) Metabolomics (LC-MS) of cells cultured on 400 or 60k ECM for 24 h; percent (%) metabolites significantly altered relative to 400 Pa ± 500 nM BIX (n = 4–5 biological replicates; LC-MS run together, repeated 2 separate times).

(F) Confocal microscopy depicting mitochondrial network structure of SLC9A1 KO cells on 60k Pa surfaces for 24 h; 100 nM MitoTracker (deep red FM). Scale bar, 10 μm. MitoMAPR quantification: WT (8) and SLC9A1 KO (21) junctions per network.

(G) Fractional contribution of $^{13}C_6$-glucose to a selection of pertinent metabolites. Two hour labeling (n = 3 biological replicates; LC-MS run together).

(H) Intracellular pH (pHi) of WT or SLC9A1 KO cells grown on soft-to-stiff ECM measured via 1 μM 2',7'-Bis-(2-carboxyethyl)-5-(and-6)-carboxyfluorescein, acetoxymethyl ester (BCECF) (n = 6 replicates, repeated 4 times, shown together).

(I) Representative microscopy depicting mitochondrial network structure of live *C. elegans*-expressing MLS::mRuby (mitochondrial matrix) grown on empty vector or *nhx-2* (*SLC9A1* ortholog) RNAi from hatch of 5- or 15-day-old animals.

Please cite this article in press as: Tharp et al., Adhesion-mediated mechanosignaling forces mitohormesis, Cell Metabolism (2021), https://doi.org/10.1016/j.cmet.2021.04.017

CellPress

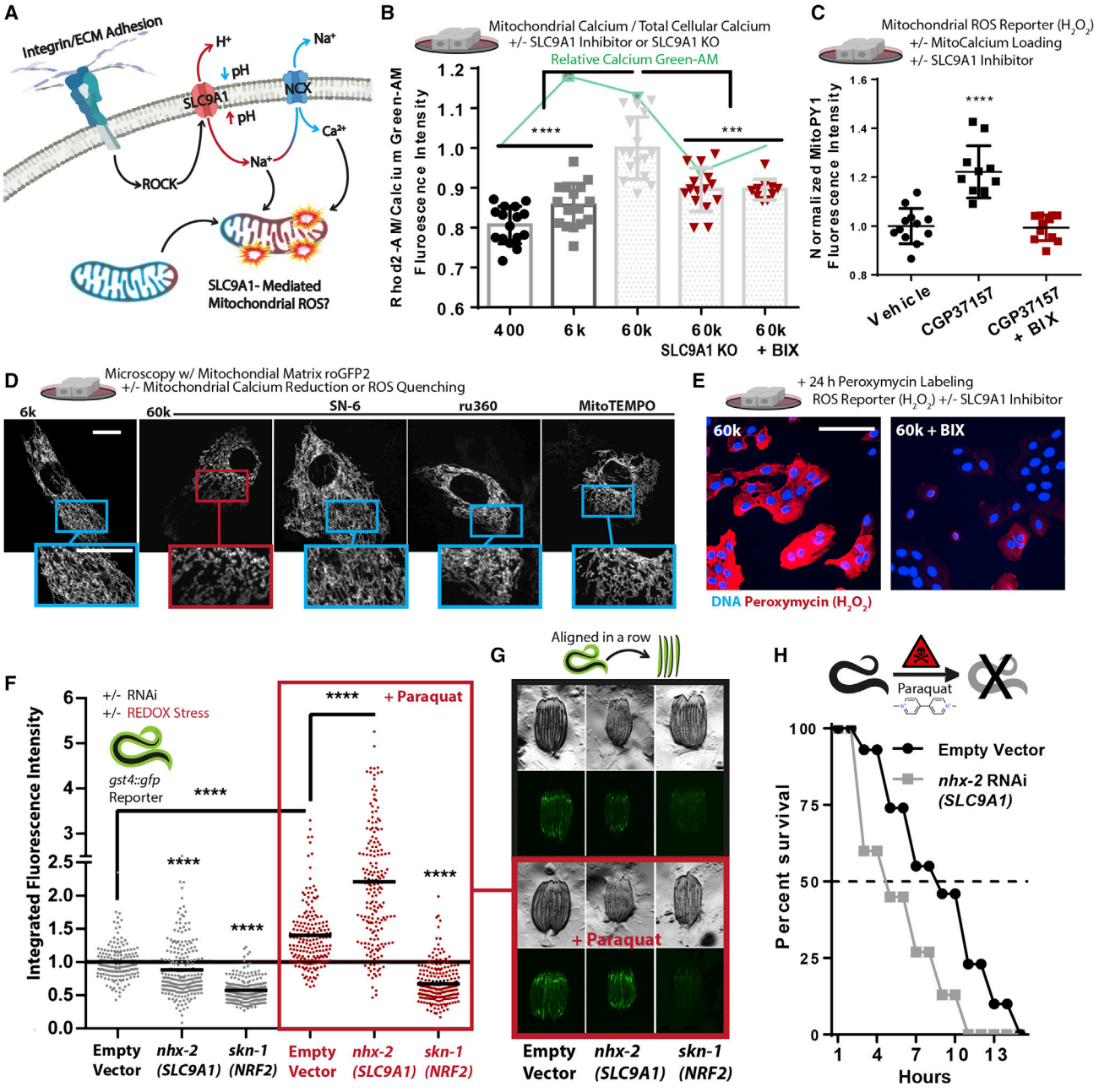

Figure 3. SLC9A1 facilitates mitochondrial oxidative stress

(A) Graphical schematic indicating how SLC9A1 affects mitochondrial oxidative stress.

(B) Calcium content of MECs cultured on soft-to-stiff ECM for 24 h, treated with 2 μM Rhod2-AM (mitochondrial) and 2 μM calcium green-1-AM (intracellular) (n = 4 replicates, repeated 4 times).

(C) Mitochondrial H_2O_2 production of cells cultured on 6k Pa surfaces and treated with 500 nM BIX or vehicle for 24 h and then 5 μM MitoPy1 and vehicle or 1 μM CGP37157 for 1 h (n = 6, repeated 2 times).

(D) Confocal microscopy depicting mitochondrial network structure of PFA-fixed MECs on 6 or 60k Pa ECM treated with 1 μM ru360 (MCU inhibitor), 10 μM SN-6 (NCX reverse mode inhibitor, opposite direction of CCP37157), and 2 μM mitoTEMPO for 24 h. Scale bar, 10 μm. MitoMAPR quantification: 6k (21), 60k (6), 60k + SN-6 (27), 60k + Ru360 (13), and 60k + MitoTEMPO (12) junctions per network.

(E) Confocal microscopy of peroxymycin (H_2O_2) (Chung et al. 2018) staining over 24 h on 60k Pa ECM ± 500 nM BIX; quantitated in Figure S3I.

(F and G) *gst-4p::gfp* reporter fluorescent intensity of *C. elegans* measured with a large particle cytometer ± 50 mM paraquat (n = 177, 206, 190, 187, 191, and 215 animals in order, left to right) with representative images (G) of *C. elegans* quantified, repeated 3 times.

(H) *C. elegans* survival in 50 mM paraquat at 1 day; animals grown from hatch on *nhx-2* RNAi versus empty-vector control (80 worms per condition, repeated 3 times).

Please cite this article in press as: Tharp et al., Adhesion-mediated mechanosignaling forces mitohormesis, Cell Metabolism (2021), https://doi.org/10.1016/j.cmet.2021.04.017

C. elegans nhx-2 knockdown was dramatically extended (Figure S3N).

Since oxidative stress primarily regulates the expression of *gst-4p* through the transcriptional activity of *skn-1* (*NRF-2* ortholog), which facilitates the canonical oxidative stress response (OSR) by prompting transcription of genes with antioxidant response elements (ARE) in their promoters (e.g., *gst-4p*), we used a knockdown of *skn-1/NRF-2* as a negative control. As a positive control, we treated the *gst-4p::gfp* reporter animals with paraquat, an herbicide that promotes mitochondrial ROS leak/production (Castello et al., 2007), which increased oxidative stress reporter activity. Surprisingly, paraquat treatment induced a more robust *gst-4p::gfp* reporter response to paraquat in *nhx-2* knockdown animals (Figures 3F and 3G). This result suggests that *nhx-2* knockdown exacerbated paraquat-induced mitochondrial oxidative stress, likely because OxPhos could not be throttled. To test the difference in oxidative stress sensitivity of *nhx-2* knockdown animals, we assayed the survival of these animals in response to paraquat-induced oxidative stress. Corroborating the *gst-4p::gfp* reporter measurements (Figures 3F and 3G), the *nhx-2* knockdown animals were more sensitive to paraquat exposure than control animals (Figure 3H). Accordingly, these results indicate that SLC9A1 activity may induce OxSR via adhesion-mediated production of sub-lethal mitochondrial ROS, which promote mitochondrial reorganization (toroid/fragment formation) and may prepare cells and animals to overcome subsequent oxidative stresses.

The greater induction of *gst-4p::gfp* and the rapidity of death observed in the *nhx-2* knockdown animals suggested that they were less adapted to manage the ROS-mediated oxidative stress induced by paraquat. Since greater SLC9A1 activity appeared to promote mitochondrial ROS production (Figures 3C, 3E, S3G, S3I, and S3J) we hypothesized that because the *nhx-2* knockdown animals experienced lower basal levels of ROS exposure, they were not pre-adapted to survive the paraquat exposure. It has been reported that mitochondrial stresses, particularly ROS production and respiratory dysfunction, promote adaptive reprogramming of mitochondrial function and OxSR through a process described as "mitohormesis" (Ma, 2013; Ristow, 2014; Yun and Finkel, 2014). In biological systems, hormesis describes a biphasic dose response in which a stress/signal is moderated by a compensatory response (Mattson, 2008). For example, cancer cells produce more ROS than healthy cells produce, but the oncogene-induced overproduction of ROS elicits compensatory ROS quenching response mediated by the transcriptional activity of NRF2 (nuclear factor erythroid-2-related factor 2). This NRF2-mediated ROS quenching OSR facilitates metabolic remodeling that provides cancer cells with OxSR requisite to harness ROS-mediated proliferation and migration effects without succumbing to ROS-mediated cell death (Reczek and Chandel, 2017). OxSR in cells and animals can be the product of NRF2-mediated OSR or other adaptive programs, which are less well defined.

Stiff ECM forces HSF1-mediated mitochondrial reprogramming

Since MECs cultured on stiff ECM experienced a greater amount of ROS stress as they adapted to the environment via integrin adhesion, we sought to determine if they had induced the NRF2-mediated OSR to survive and adapt (Figure 4A). To test this, we used RNA sequencing (RNA-seq) to characterize the transcriptional state of MECs cultured on soft-to-stiff ECM or soft ECM with hyperglycemia for 24 h. We compared the transcriptional programs induced by hyperglycemia and adhesion substrate elasticity because they both affect cytoskeletal tension, mitochondrial reorganization (fragment/toroid), and mitochondrial oxygen consumption. Unsupervised hierarchical clustering demonstrated that the greatest transcriptomic signature overlap occurred in MECs plated on the soft ECM (400 Pa) that were exposed to extreme hyperglycemia (25 mM) and MECs plated on the stiff ECM (60k Pa) with physiological glucose (5 mM) (Figure 4B). Gene ontology analysis indicated that the categories that were downregulated in response to stiff ECM included oxidation-reduction process, oxidoreductase activity, ion transport, mitochondrion, and mitochondrial inner membrane (Figure S4A). We also found that of all mitocarta 2.0 (Calvo et al., 2016) annotated mitochondrial genes encoded by the nuclear genome, which change (up or down) in response to hyperglycemia or stiff ECM, the vast majority of these changes were conserved between both stresses (Figure 4C). Specifically, a number of ETC subunits were downregulated (*NDUFA7*, *ATP5B*, *ATP5D*, *COX6b1*, etc.), while mitochondrial-localized chaperones and proteases, which facilitate mitochondrial import, protein folding, and structural remodeling of the mitochondria during UPR^{mt}, were upregulated (*YME1L1*, *HSPE1*, *DNAJC10 [hsp40]*, *HSPD1*, *HSPA9*, *HSPB11*, etc.) (Labbadia et al., 2017). With regard to NRF2 and the OSR it facilitates, unexpectedly, cells cultured on stiff ECM had downregulated many canonical ARE-containing target genes (HMOX1, TXN, GPX2, GPX4, NQ01, etc.).

It was paradoxical that genes with AREs in their promoters were not upregulated in MECs cultured on stiff ECM, since they had experienced a greater amount of redox stress. However, this result could indicate that the transcriptomes measured reflected a post OSR state, in which oxidants were not actively produced, and therefore, ARE-mediated gene expression was downregulated. To address this possibility, we compared the transcriptional signature of MECs cultured on stiff ECM with other known stress responses (Grandjean et al., 2019) that can remediate damage resulting from oxidative stress, such as protein misfolding (Reichmann et al., 2018). We found that the majority of genes, which characterize the integrated stress response (ISR), were downregulated; heat shock response (HSR) genes were upregulated; and genes ascribed to the OSR and UPR^{mt} were inconsistently up- and downregulated. However, when comparing the upregulated genes of the UPR^{mt}, OSR, and HSR, we noted that the upregulated genes associated with all of these stress responses were primarily heat shock proteins (HSPs) regulated by heat shock factor 1 (HSF1) (Table S1) (Grandjean et al., 2019).

Activation of UPR^{mt} is thought to occur in response to mitochondrial respiratory dysfunction, so we tested if integrin signaling affected the activation of the UPR^{mt} to the same degree as stiff ECM. UPR^{mt} has been most well defined in *C. elegans*, so we used an established model of cytochrome *c* oxidase-1 subunit Vb (*cco-1/COX4*) knockdown, which robustly induces a fluorescent UPR^{mt} reporter, *hsp-6::gfp* (*HSPA9*/mtHSP70 ortholog), in *C. elegans*. We performed double RNAi of *cco-1* in conjunction

Please cite this article in press as: Tharp et al., Adhesion-mediated mechanosignaling forces mitohormesis, Cell Metabolism (2021), https://doi.org/10.1016/j.cmet.2021.04.017

CellPress

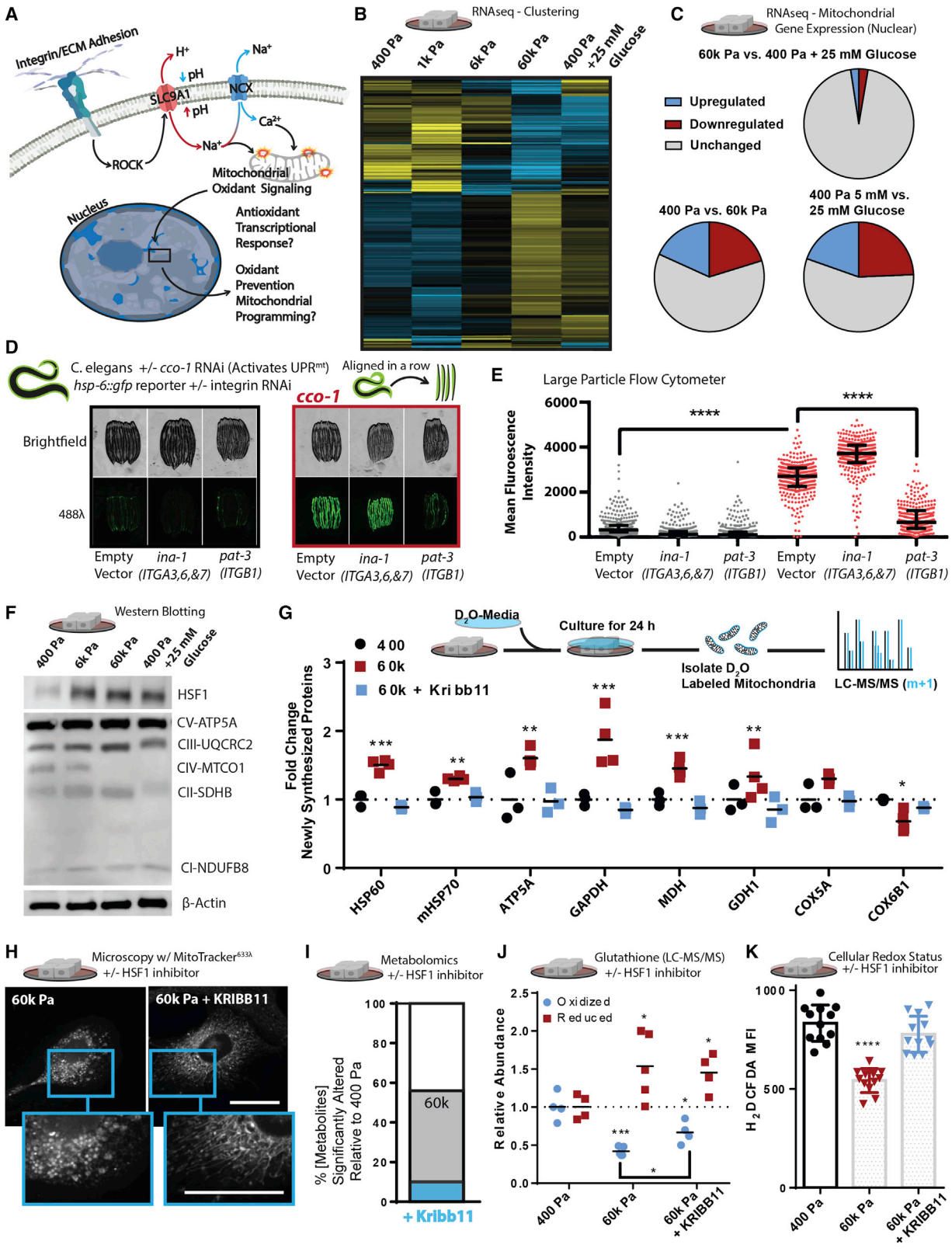

(legend on next page)

Please cite this article in press as: Tharp et al., Adhesion-mediated mechanosignaling forces mitohormesis, Cell Metabolism (2021), https://doi.org/10.1016/j.cmet.2021.04.017

with knockdown of *ina-1* (*ITGA* ortholog, most similar to *ITGA3*,*6*, and *7*) or *pat-3* (*ITGB1* ortholog). We found that *pat-3*/*ITGB1* knockdown robustly attenuated *cco1*-mediated UPR^{mt}, which suggests that integrin signaling is an important input to the activation of UPR^{mt} (Figures 4D and 4E). We then determined that HSF1 is required for the maximal activation of *cco1*-mediated UPR^{mt} in *C. elegans*, as RNAi knockdown of *hsf-1* partially suppressed UPR^{mt} induction (Figure S4B). Since *C. elegans* activate UPR^{mt} primarily through *atfs-1* (Nargund et al., 2012), which does not have a conspicuous mammalian ortholog (Fiorese et al., 2016), the data suggest that HSF1 may play a larger role in the mammalian UPR^{mt} (Katiyar et al., 2020) or may resolve a UPR^{mt}-overlapping aspect of mitochondrial dysfunction (Boos et al., 2019) that promotes OxSR.

HSF1 is primarily known to regulate a transcription program that facilitates the survival of cells experiencing heat stress (~43°C), but it may have an unappreciated role in OxSR since its transcriptional activity is regulated by ROS (H_2O_2) (Ahn and Thiele, 2003). Upregulation of HSF1 expression is an outcome of the NRF2-mediated OSR because the HSF1 promoter (−1.5k to −1.7k bp) is heavily enriched with AREs (Paul et al., 2018). Indeed, we found that HSF1 abundance increased in response to stiff ECM or hyperglycemia, as was mitochondrial ATP5A, but not the mitochondrial encoded subunit of oxygen consuming ETC complex IV subunit, MTC01 (Figure 4F). Inhibiting SLC9A1 in MECs cultured on stiff ECM repressed the expression of HSF1 and its downstream targets (Figure S4C). Treatment with MitoTEMPO, a mitochondria-targeted antioxidant, suppressed stiff ECM or paraquat-induced HSF1 and HSF1-target gene expression (Figures S4D and S4E). Overall, these data indicate that ROS induced by the stiff ECM via SLC9A1 activity promotes HSF1 expression and activity (Figures 3E and S3I).

We postulated that HSF1 could modify mitochondrial structure/function by influencing the expression of the mitochondrial import machinery, such as mtHSP70 (*HSPA9*) (Wiedemann and Pfanner, 2017), or by regulating mitochondrial biogenesis in collaboration with peroxisome-proliferator-activated receptor gamma coactivator 1-alpha (PGC-1α) (Charos et al., 2012). To test these possibilities, we measured the incorporation of newly synthesized proteins into the mitochondria with stable isotope incorporation mass spectrometry, which revealed that the stiff ECM enhanced the incorporation of newly synthesized proteins in an HSF1-dependent fashion (Figure 4G). Consistent with the hypothesis that an HSF1-mediated response facilitated the stiff ECM-induced mitochondrial adaptation, HSF1 inhibition was sufficient to prevent the altered mitochondrial morphology induced by stiff ECM (Figure 4H). Inhibition of HSF1 also restored ~80% of the metabolite concentrations measured in MECs plated on stiff ECM to that of MECs cultured on soft ECM (Figure 4I). Overall, these findings suggest that ECM mechanosignaling alters mitochondrial reorganization and metabolic programing through a heat-stress-independent HSF1-mediated program (Mendillo et al., 2012).

To explore if adhesion-mediated mechanosignaling facilitates a HSF1-dependent OxSR program, we quantified the levels of reduced and oxidized glutathione, the primary cellular oxidant detoxification and redox (reduction:oxidation) management system, which becomes oxidized in the presence of ROS. MECs cultured on stiff ECM had lower levels of oxidized glutathione than those on soft ECM. HSF1 inhibition was sufficient to significantly increase the levels of oxidized glutathione in MECs on stiff ECM (Figure 4J). Metabolomics allowed us to observe that many metabolite changes that reflect OxSR (LeBoeuf et al., 2020), such as PPP activity, which generates reduced nicotinamide adenine dinucleotide phosphate (NADPH) required to regenerate reduced glutathione and mitigate oxidative stress, were also elevated in response to stiff ECM, and could be normalized by inhibiting HSF1 (Figure S4F). Indeed, HSF1 inhibition abolished the enhanced reducing capacity of MECs that had been cultured on stiff ECM for 24 h prior to the measurement of redox stress (Figure 4K). The data indicate that while MECs experience more redox stress in response to stiff ECM, they adapt and acquire an OxSR through HSF1-dependent changes in cellular metabolism facilitated by mitochondrial reprogramming via compositional changes (Figures 1D, 4E, and 4F).

To examine how HSF1 influences mitochondrial metabolic flux, we traced the metabolic fate of isotopic glucose

Figure 4. Mechanosignaling facilitates mitochondrial stress response via HSF1

(A) Graphical representation of the paradigm and remaining questions.

(B) Heatmap depicting unsupervised hierarchical clustering of RNA-seq of cells cultured on soft-to-stiff ECM for 24 h ± 5 or 25 mM glucose (n = 2 duplicate libraries of 3 biological replicates, ~10 million reads per library).

(C) Comparison of significantly altered MitoCarta 2.0 cataloged genes from the 400 Pa, 60k, and 400 Pa + 25 mM glucose conditions shown in (B).

(D) *hsp-6::gfp* reporter fluorescent intensity representative images of *C. elegans*, quantified in (E). RNAis were mixed at a 5:1 ratio of ev, *ina-1*, or *pat-3* RNAi to ev or *cco-1* RNAi as depicted (*hsp-6* is the *HSPA9*/mtHSP70 ortholog).

(E) Quantification of *hsp-6::gfp* reporter fluorescent intensity of *C. elegans* measured with a large particle cytometer, ± *cco-1* RNAi (n = 387, 309, 377, 326, 312, and 294 animals in order, left to right, repeated 3 times).

(F) Western blot depicting relative protein abundance of HSF1, ETC components, or β-actin within 5 μg of total protein derived from lysates of MECs cultured on soft-to-stiff ECM for 24 h ± 5 or 25 mM glucose.

(G) Stable isotope mitochondrial proteomics of crude mitochondrial fraction of MECs grown 400 or 60k Pa ECM for 24 h ± 2 μM KRIBB11 (n = 4 biological replicates; LC-MS run together, repeated 2 times)

(H) Confocal microscopy of 100 nM MitoTracker (deep red FM) stained and fixed (PFA) cells cultured on 60k Pa ECM surfaces for 24 h ± vehicle or 2 μM KRIBB11. MitoMAPR quantification: 60k (7) and 60k + Kribb11 (12) junctions per network.

(I) Metabolomics (LC-MS) of cells cultured on 400 or 60k Pa ECM for 24 h; percent (%) significantly altered relative to 400 Pa ± 2 μM KRIBB11 (n = 4–5 biological replicates; LC-MS/MS run together, repeated 2 times).

(J) Oxidized/reduced glutathione (NEM protected) measurements of MECs grown on 400 or 60k Pa ECM for 24 h ± 2 μM KRIBB11 (n = 4 biological replicates, repeated two times) (n = 4–5 biological replicates; LC-MS run together, repeated 2 times).

(K) Oxidative stress indicator intensity of cells after 1 h. MECs cultured on varied 400 or 60k Pa ECM for 24 h ± vehicle or 2 μM KRIBB11, measured with 2 μM 2′,7′-dichlorodihydrofluorescein diacetate (H_2DCFDA) (n = 4, repeated 3 times, shown together).

Please cite this article in press as: Tharp et al., Adhesion-mediated mechanosignaling forces mitohormesis, Cell Metabolism (2021), https://doi.org/10.1016/j.cmet.2021.04.017

CellPress

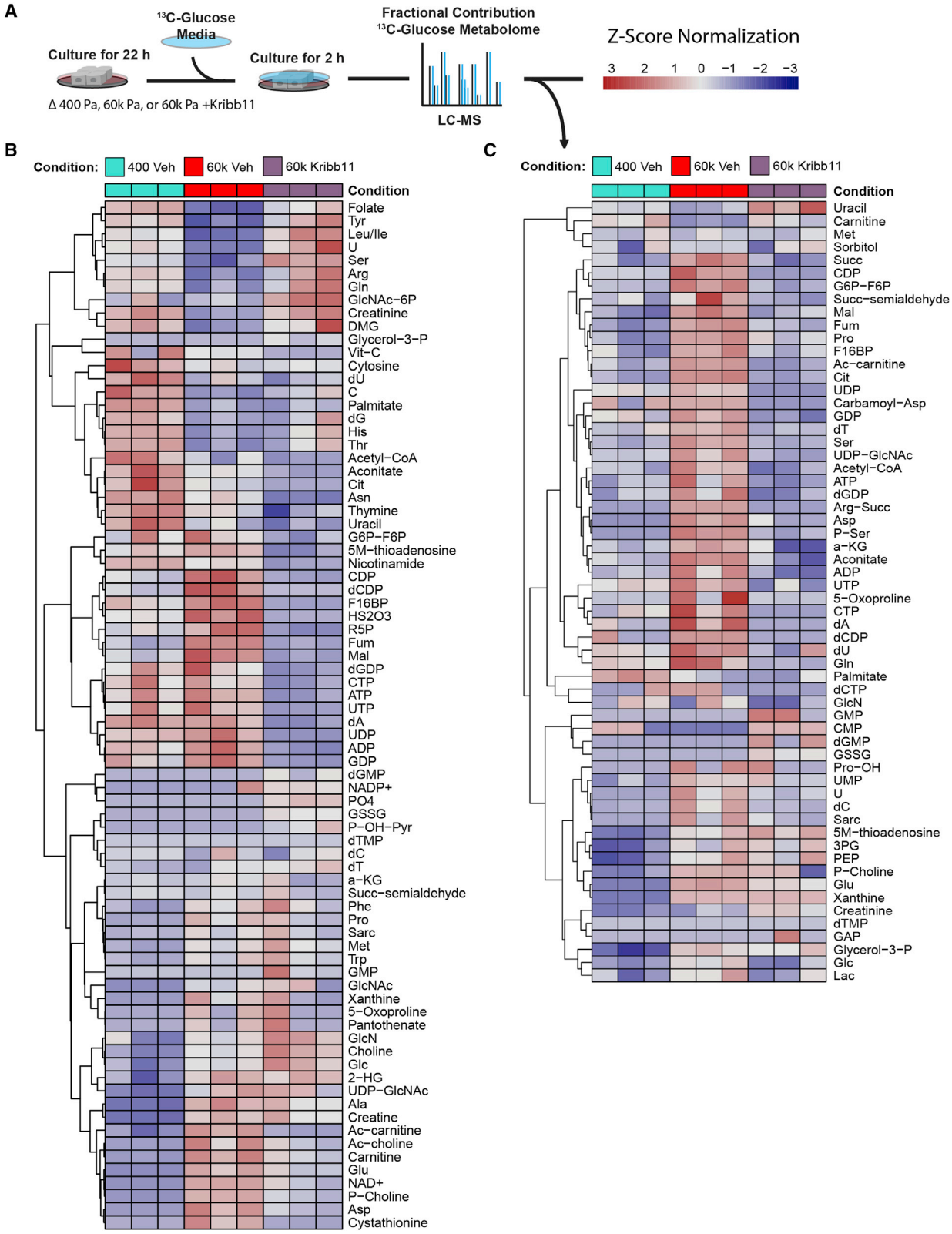

(legend on next page)

Please cite this article in press as: Tharp et al., Adhesion-mediated mechanosignaling forces mitohormesis, Cell Metabolism (2021), https://doi.org/10.1016/j.cmet.2021.04.017

metabolism in cells grown on soft or stiff ECM with or without HSF1 inhibition (Figure 5A). We allowed the cells to metabolize the labeled glucose for 2 h to ensure robust labeling of mitochondrial TCA cycle intermediates (Jang et al., 2018). Consistently, we found that stiff ECM dramatically alters the relative abundance of the whole metabolome, and also the flux of glucose metabolism (Figures 5B and 5C). Of note, we observed increases in the fractional labeling (enrichment of isotopic carbon derived from glucose) in many metabolites of the TCA cycle, urea cycle, and purine and pyrimidine metabolism pathway (Figure S5), which could indicate a concerted remodeling of metabolism to support mechanosignaling or OxSR (Figure 6A). Interestingly, the oncometabolite fumarate (Sciacovelli et al., 2016) is a metabolic intermediate between the urea cycle and the TCA cycle that may also be a driver of the altered mitochondrial morphologies observed (Crooks et al., 2021) in cells adapting to stiff ECM.

HSF1 can be pharmacologically activated using celastrol, a reactive electrophile derived from the "Thunder of God" vine (*Tripterygium wilfordii*) (Ma et al., 2015), which was sufficient to induce mitochondrial fragmentation/toroids in MECs on all substrates (Figures 6B and S6A). HSF1 activation also increased extracellular acidification rate (ECAR), a proxy measure of glycolytic flux, and reduced mitochondrial oxygen consumption (Figure 6C). A mitochondria-localized ROS (H_2O_2) reporter (MitoPY1) revealed that MECs treated with Celastrol had significantly suppressed mitochondrial ROS production (Figure 6D). Expression of a constitutively active HSF1 induced fragmented/toroidal mitochondria in MECs plated on the soft ECM (Figures 6E and S6B) and increased mitochondrial membrane potential (Figure S6C). Conversely, HSF1 knockdown increased mitochondrial respiration (Figure 6F), induced oxidative stress (Figures 6G and S5D), and decreased mitochondrial membrane potential (Figures 6H and S6E) in both the MCF10A (nonmalignant) and MDA-MB-231 (aggressive and malignant) MECs (Figures S6F–S6I). The physiological relevance of these findings was confirmed by reducing *hsf-1* expression in *C. elegans*, which decreased mitochondrial content and membrane potential throughout the whole organism (Figures 6I and 6J). This indicates that increased HSF1 activity reduces mitochondrial oxygen consumption and increases the mitochondrial membrane potential because proton flow from IMS to MM is reduced, which may limit ROS produced as a byproduct of OxPhos, mediating an enhanced OxSR by suppressing the mitochondrial contribution to net oxidative stress.

ECM mechanosignaling engenders mitochondrial OxSR via HSF1 and YME1L1

Thus far, the data suggested that adhesion-mediated mechanosignaling stimulates a heat-stress-independent HSF1 transcriptional program, previously implicated in cancer, that alters mitochondrial structure/function and restricts mitochondrial respiration and oxidant production. Accordingly, we next stress-tested if the OxSR adaptation was sufficient to oppose mitochondrial ROS-mediated apoptosis, a trait associated with many tumors (Reczek et al., 2017). We treated MECs cultured on soft-to-stiff ECM, with paraquat and assayed for apoptosis (Sprenger and Langer, 2019). Consistent with the hypothesis that mechnosignaling promotes OxSR via HSF1, MECs cultured on stiff ECM were less sensitive to paraquat treatment. This OxSR phenotype could be further enhanced via expression of constitutively active HSF1 and ablated by HSF1 knockdown or inhibition (Figures 7A, 7B, S7A, and S7B). Functional links between mechanosignaling and mitochondrial OxSR adaptation were verified by determining that mitochondrial depletion negated the impact of ECM stiffness on redox sensitivity to paraquat (Figure S6C).

Due to the fact that stiff ECM and HSF1 altered mitochondrial protein turnover rates and mitochondrial import is required for mitochondrial protein turnover, we next assessed whether cytoskeletal tension mediated OxSR was dependent upon mitochondrial protein import. Nuclear-encoded mitochondrial proteins are imported into the mitochondria (Schmidt et al., 2010), a process that requires a number HSF1 target genes to efficiently occur (e.g., *HSPD1* [HSP60], *HSPE1* [HSP10], and *HSPA9* [mtHSP70]; Deocaris et al., 2006; Schneider et al., 1994). To test if cytoskeletal tension enhanced mitochondrial import was critical for OxSR, we used JG-98, an inhibitor of HSP70 that enriches in mitochondria (Ferguson et al. 2020; Li et al., 2013; Srinivasan et al., 2018). JG-98-treated cells grown on stiff ECM were not apoptotic but were hyper-sensitized to paraquat-induced death (Figure S6D). To identify the specific mediators of the HSF1-dependent OxSR, we cross-referenced conserved nuclear-encoded mitochondrial genes containing heat shock elements (HSEs) in their promoters with genes whose expression was upregulated by cytoskeletal tension (Figure 3B). We found one likely candidate, mitochondrial escape 1 like 1 (*YME1L1*), a zinc-dependent metalloprotease of the AAA^+ protein family (ATPases with diverse cellular activity), which is a hallmark of UPR^{mt} and regulates mitochondrial morphology (MacVicar and Langer, 2016; MacVicar et al., 2019). We verified that YME1L1 protein levels were regulated by HSF1 and were upregulated in response to mechanosignaling via stiff ECM (Figures 7C and 7D).

Since HSF1 resolves mitochondrial import stress (Boos et al., 2019) by regulating the expression mitochondrial import machinery, we hypothesized that dysfunctional or ROS-producing mitochondria elicit a adaptive response to potentiate mitochondrial import capacity and facilitate the import of certain nuclear-encoded mitochondrial proteins that mediate mitochondrial repair/reprogramming (Figure 7E). To determine if YME1L1 played a role in stiff-ECM-induced OxSR, we utilized CRISPR-I to downregulate YME1L1 expression. YME1L1 knockdown sensitized MECs cultured on stiff ECM to paraquat-induced

Figure 5. HSF1 facilitates mechanosignaling-mediated metabolic reprogramming

(A) Graphical depiction of experimental design.

(B) Heatmap of relative metabolite levels of MECs cultured on 400 or 60k Pa vehicle (DMSO treated) or 60k Pa ECM with 2 μM Kribb11 for 22 h followed by media exchanged for $^{13}C_6$-glucose containing media for 2 h and then harvested for LC-MS analysis (n = 3 biological replicates).

(C) Heatmap of fractional contributions of $^{13}C_6$-glucose to the metabolome of MECs cultured on 400 Pa or 60k Pa vehicle (DMSO treated) or 60k Pa ECM with 2 μM Kribb11 over the course of 2 h. MECs were previously cultured for 22 h in the same conditions with unlabeled glucose media (n = 3 biological replicates; LC-MS analysis).

Please cite this article in press as: Tharp et al., Adhesion-mediated mechanosignaling forces mitohormesis, Cell Metabolism (2021), https://doi.org/10.1016/j.cmet.2021.04.017

CellPress

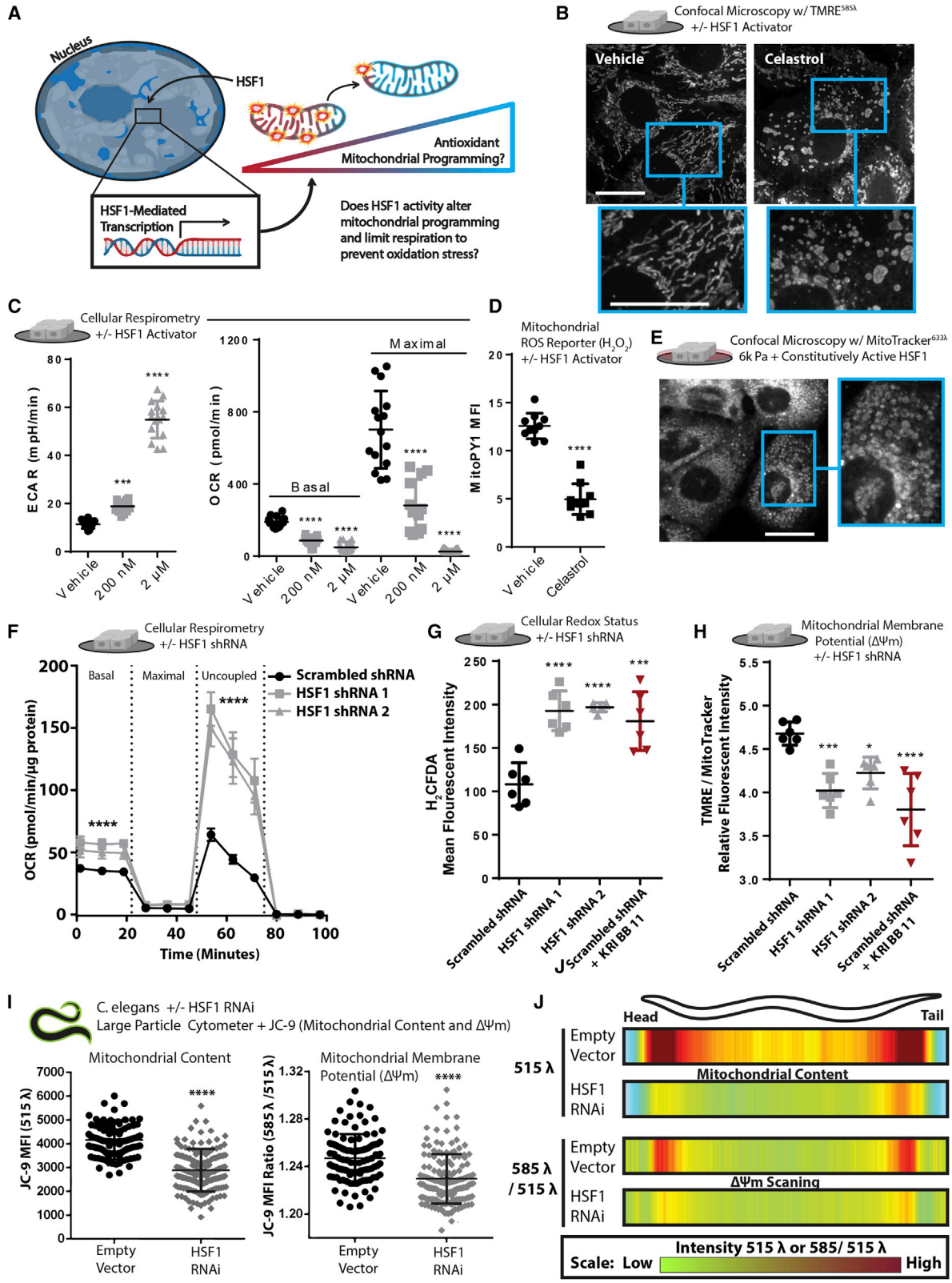

(legend on next page)

Please cite this article in press as: Tharp et al., Adhesion-mediated mechanosignaling forces mitohormesis, Cell Metabolism (2021), https://doi.org/10.1016/j.cmet.2021.04.017

death to a similar degree as cells plated on soft ECM (Figure 7F). Attenuated *YME1LI* expression in MECs increased cellular redox stress and lowered mitochondrial membrane potential (Figure 7F) and was dependent on HSF1-mediated transcription (Figure S7F). To verify that HSF1 activity conferred OxSR through YME1L1, we examined the paraquat sensitivity of *hsf-1*-overexpressing *C. elegans* with or without reduced expression of *yme-1* (*YME1L1* ortholog). Overexpression of *hsf-1* rendered *C. elegans* more resistant to paraquat-induced death, to a greater extent than that observed in other long-lived strains (e.g., daf-2 knockdown) and potentiated the *skn-1*-mediated adaptation to redox stress (Figures S7G and S7H). Impressively, *yme-1* knockdown completely abolished the OxSR conferred to *C. elegans* through the overexpression of *hsf-1* (Figure 7G). Overall, these data indicate that YME1L1 plays an essential role in the HSF1-mediated OxSR that is induced by stiff-ECM-induced adhesion-mediated mechanosignaling.

Mechanosignaling has been established as a key driver of aggressive characteristics in breast cancers (Kai et al., 2019), and HSF1 has also been identified as a key driver of aggressive characteristics of metastatic breast cancer (Mendillo et al., 2012; Santagata et al., 2011; Scherz-Shouval et al., 2014). Therefore, we sought to determine whether the fibrotic, stiffened tissue microenvironment that develops in experimental breast tumors regulates the transcriptional activity of HSF1. We examined nuclear localization of HSF1 in the murine PyMT mammary tumors excised from mice treated with and without the lysyl oxidase inhibitor (β-aminopropionitrile, BAPN), which reduces tissue fibrosis, collagen crosslinking, and stromal stiffening of mammary tumors (Mouw et al., 2014). BAPN treatment reduced tissue fibrosis (Figure S7I) and nuclear localization of HSF1 in the mammary tumor cells (Figures S7J–S7K). HSF1 and YME1L1 have been shown to be involved in many tumor types; however, breast cancer cells appear to be most dependent on HSF1 or YME1L1 (Figure S7K).

DISCUSSION

We identified a mechanism whereby the physical properties of the microenvironment alter mitochondrial composition, structure, and function to tune cellular metabolism through a mechanical stress adaptation. We demonstrate that SLC9A1 and HSF1 alter mitochondrial function to support OxSR by regulating the levels of YME1L1 (MacVicar et al., 2019). The mechano-responsiveness of HSF1 and its ability to limit mitochondrial respiration may explain why oncogene-driven Warburg metabolism has been so difficult to observe *in vitro*. The rigid tissue culture polystyrene substrates (3G Pa) elevate mechanosignaling and chronically activate HSF1, regardless of oncogene transformation, and this effect obscures any comparative measurements of mitochondrial function in normal and oncogene-transformed cells. Instead, prudent use of model systems with biomimetic properties (physically and chemically similar to the relevant biological system) is needed to uncover oncogene-driven alterations in mitochondrial metabolism (Cantor et al., 2017; DelNero et al., 2018).

Our findings here demonstrate that HSF1-driven redox management not only suppresses the production of ROS by limiting mitochondrial respiration, but it also opposes oxidant damage by promoting mitochondrial biogenesis/protein turnover and enhancing reducing equivalents (reduced glutathione/NADPH). Previous studies have indicated that cell-detachment/attachment-associated signaling elicits redox stress (Radisky et al., 2005; Schafer et al., 2009; Werner and Werb, 2002). With that in mind, coupling redox stress management to a molecular rheology sensor would be a rational design principle to promote cell survival. HSF1 is a logical candidate to serve as such a molecular rheology sensor because it facilitates cellular stress responses to the accumulation of misfolded proteins in the cytosol. Misfolded proteins can accumulate owing to changes in pH, ion concentrations, osmolality, osmotic pressure, molecular crowding, adhesion-associated forces (mechanotransduction), enthalpy (heat), entropy (order), and redox balance (Ahn and Thiele, 2003; Dill, 1990; Dill and MacCallum, 2012; Guo et al., 2017; Higuchi-Sanabria et al., 2018)—all of which are cellular conditions associated with HSF1 activation. By surveying the physical state of the proteome, HSF1 is poised to temper diverse environmental perturbations that elicit mitochondrial dysfunction and oxidant leak. Indeed, HSF1 could mitigate the redox stress induced by conditions that deform mitochondrial structure (Helle et al., 2017), such as the physical stresses cells encounter in tumors with high interstitial pressure,

Figure 6. HSF1 induces mitochondrial reprogramming

(A) Graphical depiction of experimental question.

(B) Confocal microscopy depicting morphology and mitochondrial membrane potential staining of live cells via 10 nM TMRE staining ± vehicle or 2 μM celastrol treatment for 40 min prior to imaging. MitoMAPR quantification: vehicle (10) and celastrol (6) junctions per network.

(C) Extracellular acidification rate (ECAR) and OCR of MECs treated ± vehicle or 200 nM celastrol for 24 h or 2 μM celastrol for 40 min (n = 5 wells, 3 replicate measures, repeated 3 times).

(D) Mitochondrial H_2O_2 production of cells treated with 2 μM celastrol treatment for 40 min, measured with 1 μM MitoPY (n = 5, repeated 2 times).

(E) Confocal microscopy depicting mitochondrial morphology of PFA-fixed cells expressing constitutively active HSF1 and cultured on 6k Pa ECM for 24 h, stained with 100 nM MitoTracker (deep red FM).

(F) OCR of MECs expressing a scrambled shRNA or two different shRNAs targeting HSF1 (n = 5 wells, 3 replicate measures, repeated 3 times).

(G) Oxidative stress indicator intensity after 1 h in MECs cultured on TCPS expressing a scrambled shRNA ± 2 μM KRIBB11 or two different shRNAs targeting HSF1, measured with 2 μM 2′,7′-dichlorodihydrofluorescein diacetate (H_2DCFDA) (n = 6 wells, repeated 3 times).

(H) Mitochondrial membrane potential of MECs cultured on TCPS expressing a scrambled shRNA ± 2 μM KRIBB11 or two different shRNAs targeting HSF1, measured with 1 nM TMRE and 100 nM MitoTracker after 1 h staining (n = 6, repeated 3 times).

(I) Mean fluorescent intensity of 150 per condition JC-9-stained *C. elegans* grown on empty vector or *hsf-1* RNAi from hatch, depicting mitochondrial mass (515 λ alone) or mitochondrial membrane potential (585 λ/515 λ), spatially quantified in Figure 5J.

(J) Heatmap depicting mitochondrial content (515 λ alone) or mitochondrial membrane potential (585 λ/515 λ) across the body length (head [left] to tail [right]) of 150 *C. elegans* animals grown on empty vector or *hsf-1* RNAi from hatch; JC-9 staining via administration of JC-9 loaded *C. elegans* food (*E. coli*) (repeated 3 times).

Please cite this article in press as: Tharp et al., Adhesion-mediated mechanosignaling forces mitohormesis, Cell Metabolism (2021), https://doi.org/10.1016/j.cmet.2021.04.017

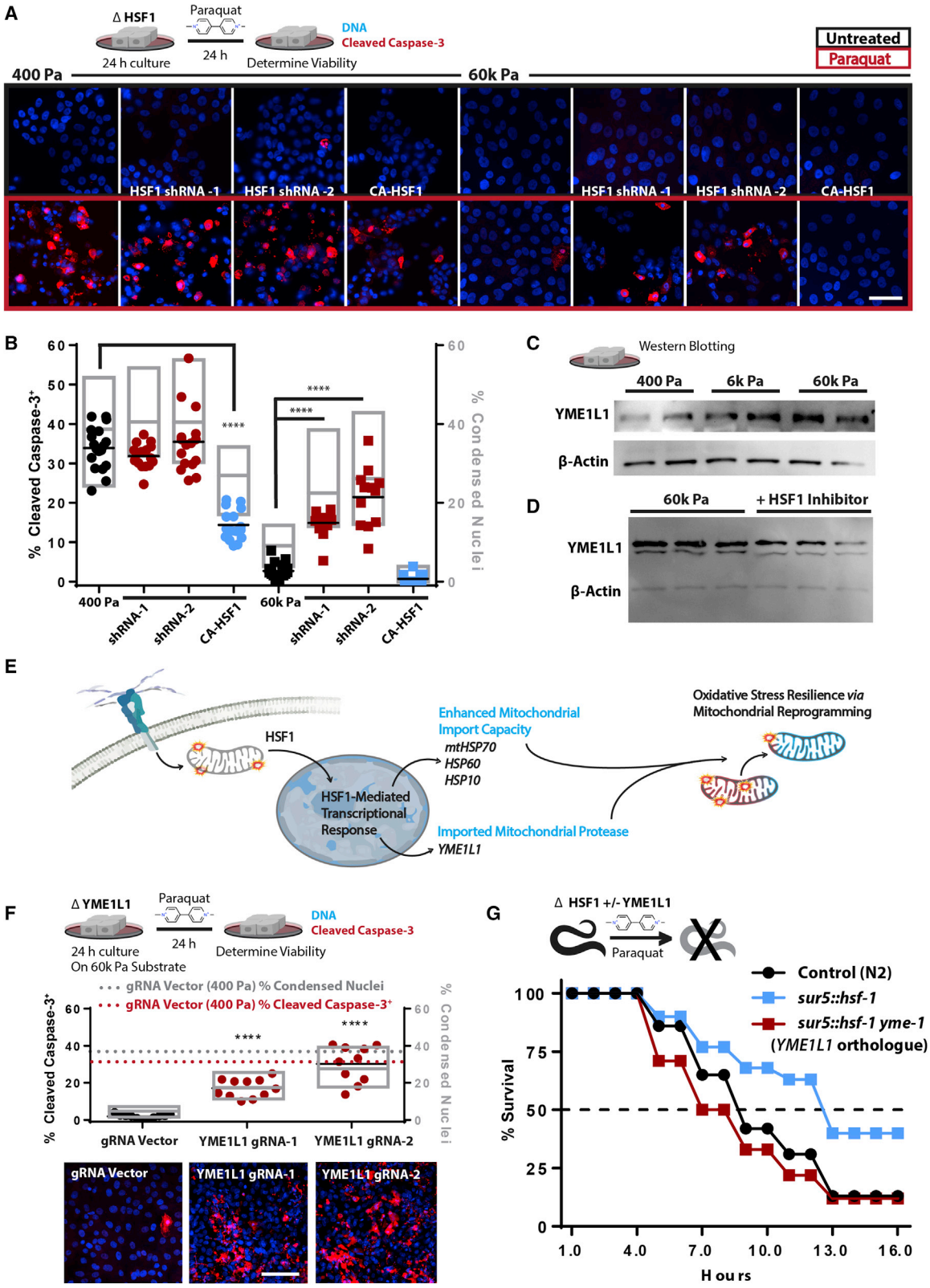

Figure 7. ECM-mediated mechanosignaling controls OxSR via HSF1 and YME1L1

(A) Confocal microscopy of indicators of apoptosis with cleaved caspase-3 staining (red) and nuclear condensation (DAPI) of MECs cultured on 400 or 60k Pa ECM for 24 h with subsequent 24 h ± 10 mM paraquat treatment. 100k cells/well of 24-well plate (n = 4 replicates, repeated 3 separate times).

(legend continued on next page)

Please cite this article in press as: Tharp et al., Adhesion-mediated mechanosignaling forces mitohormesis, Cell Metabolism (2021), https://doi.org/10.1016/j.cmet.2021.04.017

mechanically stressful metastatic sites (Hassell et al., 2017), rigid ECMs, or oncogene-induced ROCK activity (Irianto et al., 2016; Isermann and Lammerding, 2017; Samuel et al., 2011).

HSF1 levels are elevated in the majority of tumors and are implicated in cancer aggression and metastasis (Mendillo et al., 2012; Santagata et al., 2011; Scherz-Shouval et al., 2014). Because tumors are stiffer than healthy adjacent tissues, our findings offer a tractable explanation for why HSF1 and its target genes are so frequently upregulated in tumors (Acerbi et al., 2015; Maller et al., 2021). The heat-shock-independent activation of HSF1 and its target genes would provide the tumor cells with a metabolic adaptation to this chronic mechanical stress. Since metastatic cancer cells require redox stress management adaptations to disseminate to metastatic sites (Faubert et al., 2020) and ECM stiffness promotes metastasis (Kai et al., 2019; Levental et al., 2009), our findings may describe an important molecular mechanism by which ECM tension promotes metastatic disease. In this regard, therapeutic approaches to disrupt HSF1 and its target genes have focused on cytosolic and nuclear targets but can incur difficult-to-tolerate systemic effects in humans (Dai and Sampson, 2016). We postulate that targeting the specific mediators (e.g., YME1L1, HSP60, mtHSP70, etc.) of the metabolic adaptations conferred by HSF1 could be more tractable anti-tumor therapeutic (MacVicar et al., 2019) than inhibition of HSF1 directly. Overall, our data demonstrate that the physical properties of the microenvironment play a critical role in facilitating adaptive stress responses that may contribute to metastatic characteristics of solid tumors (Faubert et al., 2020) or altered metabolism and pathology observed structurally altered tissues (e.g., aged or fibrotic).

Limitations of study

Our studies reveal a critical role for HSF1 in OxSR; however, other HSFs (e.g., HSF2) may be involved in regulating these phenotypes (Östling et al., 2007). We performed our *in vitro* experiments with DMEM:F12- or DMEM-based media classically used to culture our chosen cell line models. However, we strongly believe that our experiments would be more informative if we were to use the human-plasma-like medium (HPLM) (Cantor, 2019; Cantor et al., 2017; Rossiter et al., 2020). It is clear that the biochemical milieu influences metabolic programing, especially mitochondrial function. We hope to incorporate HPLM in our future work to more faithfully model cellular metabolic responses to physical cues in the cellular microenvironment. In this manuscript, we have demonstrated that extreme hyperglycemia affects cellular mechanosignaling and metabolic adaptations. We postulate that physiologically irrelevant glucose concentrations found in DMEM are likely one of many metabolic substrates that obfuscate our ability to translate *in vitro* findings to *in vivo* models or clinical success.

STAR★METHODS

Detailed methods are provided in the online version of this paper and include the following:

- KEY RESOURCES TABLE
- RESOURCE AVAILABILITY
  - Lead contact
  - Materials availability
  - Data and code availability
- EXPERIMENTAL MODEL AND SUBJECT DETAILS
  - Human cell culture
  - Murine mammary tumor model
  - *C. elegans* strains and maintenance
- METHOD DETAILS
  - ECM coated polyacrylamide hydrogel cell culture surfaces (PA-gels)
  - Immunofluorescence microscopy
  - MitoTacker staining
  - TMRE, H2DCFDA, Rhod-2 AM, Fura-2 AM, Calcium Green-1 AM, and MitoPy1
  - Intracellular pH (pH_i)
  - qPCR
  - Western blotting
  - MTS-roGFP2
  - V737N β1 integrin
  - WT β1 integrin
  - YME1L1 CRISPR-I
- *IN VITRO* RESPIROMETRY
  - Atomic force microscopy
  - SLC9A1 KO
  - *C. elegans* compound microscopy of mitochondria
  - *C. elegans* Paraquat survival assay
  - *C. elegans* stereomicroscopy for fluorescent transcriptional reporters
  - *C. elegans* biosorter analysis
  - Lifespan assay
  - Lattice light sheet microscopy
  - Fractal dimension and lacunarity
  - RNAseq
  - Mitochondrial ETC proteomics timsTOF
  - LC-MS/MS deuterium incorporation proteomics
  - LC-MS metabolomics

(B) Quantitation of cells from 16 field views depicted in (G) for condensed nuclei and cleaved caspase-3-positive cells (1,653–575 cells counted per condition, repeated 3 times).
(C) Western blot of YME1L1 and β-actin from 5 μg of protein derived from cells cultured on soft-to-stiff ECM for 24 h (2 biological replicates shown, repeated 3 times).
(D) Western blot of YME1L1 and β-actin from 5 μg of protein derived from cells cultured on 60k Pa ECM for 24 h ± 2 μM KRIBB11 (3 biological replicates shown, repeated 2 times).
(E) Graphical representation of the conceptual paradigm pertaining to this figure.
(F) Quantitation of MECs with YME1L1 knockdown via CRISPR-I compared with CRISPR-I and empty guide vector expressing cells on 400 Pa (dashed lines) or 60k Pa ECM, 11 field views quantified for condensed nuclei and cleaved caspase-3-positive cells (923–2,880 cells counted per condition, repeated 3 times).
(G) *C. elegans* survival in 50 mM paraquat, with *C. elegans* overexpressing *hsf-1* (*sur-5p::hsf-1*) compared or control line (N2) grown on either empty vector or *ymel-1* RNAi from hatch (n = 80 animals per condition, repeated 3 times).

- ^{13}C6-glucose LC-MS metabolomics
- Paraquat survival

- QUANTIFICATION AND STATISTICAL ANALYSIS

SUPPLEMENTAL INFORMATION

Supplemental information can be found online at https://doi.org/10.1016/j.cmet.2021.04.017.

ACKNOWLEDGMENTS

We thank the following people for their support and advice: Diane Barber and Yi Liu provided advice and reagents pertaining to SLC9A1 and pH regulation; Milos Simic generated the constitutively active HSF1; Gilberto Garcia developed the MLS mRuby *C. elegans* strain; Todd McDevitt, Serah Kang, and Ariel Kauss provided editorial suggestions that significantly improved the quality of the manuscript; Chris Chang and Yik Sham (Clive) Chung provided us with Peroxymycin to use in experiments; Michael McManus and Olga Gulyaeva provided CRISPR-I vectors; Chris Phillart maintained the cellular respirometer used in these studies; Brant Webster generated the MTS-roGFP2 vector; Fui Boon Kai acquired the ROCK:ER construct and generated the ROCK:ER stable cell line; and Bram Piersma provided dry Dutch humor, beneficial laboratory ambiance, and conversation critical to the development of this manuscript. This work was supported by 1F32CA236156-01A1, 5T32CA108462-15, and Sandler Program for Breakthrough Biomedical Research (postdoctoral independence award) to K.M.T.; R35 CA242447-01A1, R01CA192914, and R01CA222508-01 to V.M.W.; U54 CA210184 to Claudia Fischbach; 1K99AG065200-01A1 and the Glenn Foundation for Medical Research Postdoctoral Fellowship to R.H.-S.; American Diabetes Association 1-19-PDF-058 to G.A.T.; 1R01AG055891-01 and Howard Hughes Medical Institute support to A.D.; R01AG059751 to N.J.K. and D.L.S.; and National Institutes of Health (NIH) shared instrumentation grant S10 OD016387.

AUTHOR CONTRIBUTIONS

Conceptualization, K.M.T. and V.M.W.; methodology, K.M.T., R.H.-S., G.A.T., C.G.-C., B.F., A.R.D., V.M.W., A.D., and J.t.H.; investigation, K.M.T., R.H.-S., G.A.T., C.G.-C., B.F., C. Schneider, J.M.M., C. Stashko, J.R.D., S.S.M., K.-H.C., and J.t.H.; formal analysis, K.M.T., R.H.-S., G.A.T., B.F., A.L.R., D.L.S., C. Schneider, J.M.M., C. Stashko, J.R.D., S.S.M., and J.t.H.; data curation, K.M.T.; funding acquisition, V.M.W., K.M.T, A.D., M.H., D.K.N., A.R.D., K.S., J.G., D.L.S., and N.J.K.; project administration, K.M.T.; resources, V.M.W., K.M.T, A.D., M.H., D.K.N., A.R.D., K.S., H.S., and J.G.; software, C. Stashko and P.A.F.; supervision, V.M.W., A.D., K.S., A.R.D., D.K.N., D.L.S., M.H., and J.G.; validation, K.M.T., R.H.-S., G.A.T., A.S.M., C.G.-C., and C. Stashko; visualization, K.M.T.; writing – original draft, K.M.T.; writing – review & editing, V.M.W., K.M.T., A.R.D., J.R.D., R.H.-S., G.A.T., A.S.M, C.G.-C., J.M.M., C. Stashko, and S.S.M.

DECLARATION OF INTERESTS

The authors declare no competing interests.

Received: October 23, 2020
Revised: February 9, 2021
Accepted: April 26, 2021
Published: May 20, 2021

REFERENCES

Acerbi, I., Cassereau, L., Dean, I., Shi, Q., Au, A., Park, C., Chen, Y.Y., Liphardt, J., Hwang, E.S., and Weaver, V.M. (2015). Human breast cancer invasion and aggression correlates with ECM stiffening and immune cell infiltration. Integr. Biol. (Camb) *7*, 1120–1134.

Ahn, S.G., and Thiele, D.J. (2003). Redox regulation of mammalian heat shock factor 1 is essential for Hsp gene activation and protection from stress. Genes Dev *17*, 516–528.

Aldridge, J.E., Horibe, T., and Hoogenraad, N.J. (2007). Discovery of genes activated by the mitochondrial unfolded protein response (mtUPR) and cognate promoter elements. PLoS One *2*, e874.

Anesti, V., and Scorrano, L. (2006). The relationship between mitochondrial shape and function and the cytoskeleton. Biochim. Biophys. Acta *1757*, 692–699.

Baird, N.A., Douglas, P.M., Simic, M.S., Grant, A.R., Moresco, J.J., Wolff, S.C., Yates, J.R., 3rd, Manning, G., and Dillin, A. (2014). HSF-1-mediated cytoskeletal integrity determines thermotolerance and life span. Science *346*, 360–363.

Balaban, R.S., Nemoto, S., and Finkel, T. (2005). Mitochondria, oxidants, and aging. Cell *120*, 483–495.

Barasa, A., Godina, G., Buffa, P., and Pasquali-Ronchetti, I. (1973). Biochemical lesions of respiratory enzymes and configurational changes of mitochondria in vivo. I. The effect of fluoroacetate: a study by phase-contrast microscopy and time-lapse cinemicrography. Z. Zellforsch. Mikrosk. Anat. *138*, 187–210.

Boos, F., Krämer, L., Groh, C., Jung, F., Haberkant, P., Stein, F., Wollweber, F., Gackstatter, A., Zöller, E., van der Laan, M., et al. (2019). Mitochondrial protein-induced stress triggers a global adaptive transcriptional programme. Nat. Cell Biol. *21*, 442–451.

Brookes, P.S., Yoon, Y., Robotham, J.L., Anders, M.W., and Sheu, S.S. (2004). Calcium, ATP, and ROS: a mitochondrial love-hate triangle. Am. J. Physiol. Cell Physiol. *287*, C817–C833.

Butcher, D.T., Alliston, T., and Weaver, V.M. (2009). A tense situation: forcing tumour progression. Nat. Rev. Cancer *9*, 108–122.

Caliari, S.R., and Burdick, J.A. (2016). A practical guide to hydrogels for cell culture. Nat. Methods *13*, 405–414.

Calvo, S.E., Clauser, K.R., and Mootha, V.K. (2016). MitoCarta2.0: an updated inventory of mammalian mitochondrial proteins. Nucleic Acids Res *44*, D1251–D1257.

Cantor, J.R. (2019). The rise of physiologic media. Trends Cell Biol *29*, 854–861.

Cantor, J.R., Abu-Remaileh, M., Kanarek, N., Freinkman, E., Gao, X., Louissaint, A., Jr., Lewis, C.A., and Sabatini, D.M. (2017). Physiologic medium rewires cellular metabolism and reveals uric acid as an endogenous inhibitor of UMP synthase. Cell *169*, 258–272.e17.

Castello, P.R., Drechsel, D.A., and Patel, M. (2007). Mitochondria are a major source of paraquat-induced reactive oxygen species production in the brain. J. Biol. Chem. *282*, 14186–14193.

Charos, A.E., Reed, B.D., Raha, D., Szekely, A.M., Weissman, S.M., and Snyder, M. (2012). A highly integrated and complex PPARGC1A transcription factor binding network in HepG2 cells. Genome Res *22*, 1668–1679.

Chen, B.-C., Legant, W.R., Wang, K., Shao, L., Milkie, D.E., Davidson, M.W., Janetopoulos, C., Wu, X.S., Hammer, J.A., 3rd, Liu, Z., et al. (2014). Lattice light-sheet microscopy: imaging molecules to embryos at high spatiotemporal resolution. Science *346*, 1257998.

Choi, C.H., Webb, B.A., Chimenti, M.S., Jacobson, M.P., and Barber, D.L. (2013). pH sensing by FAK-His58 regulates focal adhesion remodeling. J. Cell Biol. *202*, 849–859.

Choi, M., Chang, C.Y., Clough, T., Broudy, D., Killeen, T., MacLean, B., and Vitek, O. (2014). MSstats: an R package for statistical analysis of quantitative mass spectrometry-based proteomic experiments. Bioinformatics *30*, 2524–2526.

Chung, C.Y.S., Timblin, G.A., Saijo, K., and Chang, C.J. (2018). Versatile histochemical approach to detection of hydrogen peroxide in cells and tissues based on puromycin staining. J. Am. Chem. Soc. *140*, 6109–6121.

Cox, J., and Mann, M. (2008). MaxQuant enables high peptide identification rates, individualized p.p.b.-range mass accuracies and proteome-wide protein quantification. Nat. Biotechnol. *26*, 1367–1372.

Croft, D.R., and Olson, M.F. (2006). Conditional regulation of a ROCK-estrogen receptor fusion protein. Methods Enzymol *406*, 541–553.

Crooks, D.R., Maio, N., Lang, M., Ricketts, C.J., Vocke, C.D., Gurram, S., Turan, S., Kim, Y.-Y., Cawthon, G.M., Sohelian, F., et al. (2021).

Mitochondrial DNA alterations underlie an irreversible shift to aerobic glycolysis in fumarate hydratase-deficient renal cancer. Sci. Signal. *14*, eabc4436.

Dai, C., and Sampson, S.B. (2016). HSF1: guardian of proteostasis in cancer. Trends Cell Biol *26*, 17–28.

Daniele, J.R., Esping, D.J., Garcia, G., Parsons, L.S., Arriaga, E.A., and Dillin, A. (2017). High-throughput characterization of region-specific mitochondrial function and morphology. Sci. Rep. *7*, 6749.

DelNero, P., Hopkins, B.D., Cantley, L.C., and Fischbach, C. (2018). Cancer metabolism gets physical. Sci. Transl. Med. *10*, eaaq1011.

Deocaris, C.C., Kaul, S.C., and Wadhwa, R. (2006). On the brotherhood of the mitochondrial chaperones mortalin and heat shock protein 60. Cell Stress Chaperones *11*, 116–128.

Dill, K.A. (1990). Dominant forces in protein folding. Biochemistry *29*, 7133–7155.

Dill, K.A., and MacCallum, J.L. (2012). The protein-folding problem, 50 years on. Science *338*, 1042–1046.

Dobin, A., Davis, C.A., Schlesinger, F., Drenkow, J., Zaleski, C., Jha, S., Batut, P., Chaisson, M., and Gingeras, T.R. (2013). STAR: ultrafast universal RNA-seq aligner. Bioinformatics *29*, 15–21.

Eisen, M.B., Spellman, P.T., Brown, P.O., and Botstein, D. (1998). Cluster analysis and display of genome-wide expression patterns. Proc. Natl. Acad. Sci. USA *95*, 14863–14868.

Fane, M., and Weeraratna, A.T. (2020). How the ageing microenvironment influences tumour progression. Nat. Rev. Cancer *20*, 89–106.

Faubert, B., Solmonson, A., and DeBerardinis, R.J. (2020). Metabolic reprogramming and cancer progression. Science *368*, eaaw5473.

Ferguson, I.D., Lin, Y.-H.T., Lam, C., Shao, H., Hale, M., Tharp, K.M., Mariano, M.C., Steri, V., Wang, D., Phojanokong, P., et al. (2020). Allosteric HSP70 inhibitors perturb mitochondrial proteostasis and overcome proteasome inhibitor resistance in multiple myeloma. bioRxiv. https://doi.org/10.1101/2020.04.21.052456.

Fiorese, C.J., Schulz, A.M., Lin, Y.F., Rosin, N., Pellegrino, M.W., and Haynes, C.M. (2016). The transcription factor ATF5 mediates a mammalian mitochondrial UPR. Curr. Biol. *26*, 2037–2043.

Giorgi, C., Marchi, S., and Pinton, P. (2018). The machineries, regulation and cellular functions of mitochondrial calcium. Nat. Rev. Mol. Cell Biol. *19*, 713–730.

Giustarini, D., Dalle-Donne, I., Milzani, A., Fanti, P., and Rossi, R. (2013). Analysis of GSH and GSSG after derivatization with N-ethylmaleimide. Nat. Protoc. *8*, 1660–1669.

Grandjean, J.M.D., Plate, L., Morimoto, R.I., Bollong, M.J., Powers, E.T., and Wiseman, R.L. (2019). Deconvoluting stress-responsive proteostasis signaling pathways for pharmacologic activation using targeted RNA sequencing. ACS Chem. Biol. *14*, 784–795.

Guo, M., Pegoraro, A.F., Mao, A., Zhou, E.H., Arany, P.R., Han, Y., Burnette, D.T., Jensen, M.H., Kasza, K.E., Moore, J.R., et al. (2017). Cell volume change through water efflux impacts cell stiffness and stem cell fate. Proc. Natl. Acad. Sci. USA *114*, E8618–E8627.

Hassell, B.A., Goyal, G., Lee, E., Sontheimer-Phelps, A., Levy, O., Chen, C.S., and Ingber, D.E. (2017). Human organ chip models recapitulate orthotopic lung cancer growth, therapeutic responses, and tumor dormancy in vitro. Cell Rep *21*, 508–516.

Helle, S.C.J., Feng, Q., Aebersold, M.J., Hirt, L., Grüter, R.R., Vahid, A., Sirianni, A., Mostowy, S., Snedeker, J.G., Šarić, A., et al. (2017). Mechanical force induces mitochondrial fission. eLife *6*, e30292.

Hernansanz-Agustín, P., Choya-Foces, C., Carregal-Romero, S., Ramos, E., Oliva, T., Villa-Piña, T., Moreno, L., Izquierdo-Álvarez, A., Cabrera-García, J.D., Cortés, A., et al. (2020). Na+ controls hypoxic signalling by the mitochondrial respiratory chain. Nature *586*, 287–291.

Higuchi-Sanabria, R., Frankino, P.A., Paul, J.W., 3rd, Tronnes, S.U., and Dillin, A. (2018). A futile battle? Protein quality control and the stress of aging. Dev. Cell *44*, 139–163.

Irianto, J., Pfeifer, C.R., Bennett, R.R., Xia, Y., Ivanovska, I.L., Liu, A.J., Greenberg, R.A., and Discher, D.E. (2016). Nuclear constriction segregates mobile nuclear proteins away from chromatin. Mol. Biol. Cell *27*, 4011–4020.

Isermann, P., and Lammerding, J. (2017). Consequences of a tight squeeze: nuclear envelope rupture and repair. Nucleus *8*, 268–274.

Jang, C., Chen, L., and Rabinowitz, J.D. (2018). Metabolomics and isotope tracing. Cell *173*, 822–837.

Jimenez-Blasco, D., Busquets-Garcia, A., Hebert-Chatelain, E., Serrat, R., Vicente-Gutierrez, C., Ioannidou, C., Gómez-Sotres, P., Lopez-Fabuel, I., Resch-Beusher, M., Resel, E., et al. (2020). Glucose metabolism links astroglial mitochondria to cannabinoid effects. Nature *583*, 603–608.

Kai, F., Drain, A.P., and Weaver, V.M. (2019). The extracellular matrix modulates the metastatic journey. Dev. Cell *49*, 332–346.

Katiyar, A., Fujimoto, M., Tan, K., Kurashima, A., Srivastava, P., Okada, M., Takii, R., and Nakai, A. (2020). HSF1 is required for induction of mitochondrial chaperones during the mitochondrial unfolded protein response. FEBS Open Bio *10*, 1135–1148.

Labbadia, J., Brielmann, R.M., Neto, M.F., Lin, Y.F., Haynes, C.M., and Morimoto, R.I. (2017). Mitochondrial stress restores the heat shock response and prevents proteostasis collapse during aging. Cell Rep *21*, 1481–1494.

Ladiges, W., Wanagat, J., Preston, B., Loeb, L., and Rabinovitch, P. (2010). A mitochondrial view of aging, reactive oxygen species and metastatic cancer. Aging Cell *9*, 462–465.

Lambert, T. (2019). tlambert03/LLSpy: lattice light-sheet post-processing utility. Zenodo https://github.com/tlambert03/LLSpy.

LeBoeuf, S.E., Wu, W.L., Karakousi, T.R., Karadal, B., Jackson, S.R., Davidson, S.M., Wong, K.K., Koralov, S.B., Sayin, V.I., and Papagiannakopoulos, T. (2020). Activation of oxidative stress response in cancer generates a druggable dependency on exogenous non-essential amino acids. Cell Metab *31*, 339–350.e4.

Lennon, F.E., Cianci, G.C., Kanteti, R., Riehm, J.J., Arif, Q., Poroyko, V.A., Lupovitch, E., Vigneswaran, W., Husain, A., Chen, P., et al. (2016). Unique fractal evaluation and therapeutic implications of mitochondrial morphology in malignant mesothelioma. Sci. Rep. *6*, 24578.

Levental, K.R., Yu, H., Kass, L., Lakins, J.N., Egeblad, M., Erler, J.T., Fong, S.F.T., Csiszar, K., Giaccia, A., Weninger, W., et al. (2009). Matrix crosslinking forces tumor progression by enhancing integrin signaling. Cell *139*, 891–906.

Li, X., Srinivasan, S.R., Connarn, J., Ahmad, A., Young, Z.T., Kabza, A.M., Zuiderweg, E.R.P., Sun, D., and Gestwicki, J.E. (2013). Analogs of the allosteric heat shock Protein 70 (Hsp70) inhibitor, MKT-077, as anti-cancer agents. ACS Med. Chem. Lett. *4*, 1042–1047.

Lin, Y.F., and Haynes, C.M. (2016). Metabolism and the UPR(mt). Mol. Cell *61*, 677–682.

Lin, Y.C., Jhunjhunwala, S., Benner, C., Heinz, S., Welinder, E., Mansson, R., Sigvardsson, M., Hagman, J., Espinoza, C.A., Dutkowski, J., et al. (2010). A global network of transcription factors, involving E2A, EBF1 and FoxO1, that orchestrates B cell fate. Nat. Immunol. *11*, 635–643.

Lin, G.L., Cohen, D.M., Desai, R.A., Breckenridge, M.T., Gao, L., Humphries, M.J., and Chen, C.S. (2013). Activation of beta 1 but not beta 3 integrin increases cell traction forces. FEBS Lett *587*, 763–769.

Lindström, P., and Sehlin, J. (1984). Effect of glucose on the intracellular pH of pancreatic islet cells. Biochem. J. *218*, 887–892.

Liu, X., and Hajnóczky, G. (2011). Altered fusion dynamics underlie unique morphological changes in mitochondria during hypoxia-reoxygenation stress. Cell Death Differ *18*, 1561–1572.

Liu, S., Mlodzianoski, M.J., Hu, Z., Ren, Y., McElmurry, K., Suter, D.M., and Huang, F. (2017). sCMOS noise-correction algorithm for microscopy images. Nat. Methods *14*, 760–761.

Louie, S.M., Grossman, E.A., Crawford, L.A., Ding, L., Camarda, R., Huffman, T.R., Miyamoto, D.K., Goga, A., Weerapana, E., and Nomura, D.K. (2016). GSTP1 is a driver of triple-negative breast cancer cell metabolism and pathogenicity. Cell Chem. Biol. *23*, 567–578.

Ma, Q. (2013). Role of nrf2 in oxidative stress and toxicity. Annu. Rev. Pharmacol. Toxicol. *53*, 401–426.

Ma, X., Xu, L., Alberobello, A.T., Gavrilova, O., Bagattin, A., Skarulis, M., Liu, J., Finkel, T., and Mueller, E. (2015). Celastrol protects against obesity and metabolic dysfunction through activation of a HSF1-PGC1α transcriptional axis. Cell Metab *22*, 695–708.

MacVicar, T., and Langer, T. (2016). OPA1 processing in cell death and disease - the long and short of it. J. Cell Sci. *129*, 2297–2306.

MacVicar, T., Ohba, Y., Nolte, H., Mayer, F.C., Tatsuta, T., Sprenger, H.G., Lindner, B., Zhao, Y., Li, J., Bruns, C., et al. (2019). Lipid signalling drives proteolytic rewiring of mitochondria by YME1L. Nature *575*, 361–365.

Maller, O., Drain, A.P., Barrett, A.S., Borgquist, S., Ruffell, B., Zakharevich, I., Pham, T.T., Gruosso, T., Kuasne, H., Lakins, J.N., et al. (2021). Tumour-associated macrophages drive stromal cell-dependent collagen crosslinking and stiffening to promote breast cancer aggression. Nat. Mater. *20*, 548–559.

Manor, U., Bartholomew, S., Golani, G., Christenson, E., Kozlov, M., Higgs, H., Spudich, J., and Lippincott-Schwartz, J. (2015). A mitochondria-anchored isoform of the actin-nucleating spire protein regulates mitochondrial division. eLife *4*, e08828.

Mattson, M.P. (2008). Hormesis defined. Ageing Res. Rev. *7*, 1–7.

Meier, F., Brunner, A.D., Koch, S., Koch, H., Lubeck, M., Krause, M., Goedecke, N., Decker, J., Kosinski, T., Park, M.A., et al. (2018). Online parallel accumulation-serial fragmentation (PASEF) with a novel trapped ion mobility mass spectrometer. Mol. Cell. Proteomics *17*, 2534–2545.

Mendillo, M.L., Santagata, S., Koeva, M., Bell, G.W., Hu, R., Tamimi, R.M., Fraenkel, E., Ince, T.A., Whitesell, L., and Lindquist, S. (2012). HSF1 drives a transcriptional program distinct from heat shock to support highly malignant human cancers. Cell *150*, 549–562.

Miroshnikova, Y.A., Mouw, J.K., Barnes, J.M., Pickup, M.W., Lakins, J.N., Kim, Y., Lobo, K., Persson, A.I., Reis, G.F., McKnight, T.R., et al. (2016). Tissue mechanics promote IDH1-dependent HIF1α-tenascin C feedback to regulate glioblastoma aggression. Nat. Cell Biol. *18*, 1336–1345.

Miyazono, Y., Hirashima, S., Ishihara, N., Kusukawa, J., Nakamura, K.I., and Ohta, K. (2018). Uncoupled mitochondria quickly shorten along their long axis to form indented spheroids, instead of rings, in a fission-independent manner. Sci. Rep. *8*, 350.

Moore, A.S., Wong, Y.C., Simpson, C.L., and Holzbaur, E.L.F. (2016). Dynamic actin cycling through mitochondrial subpopulations locally regulates the fission-fusion balance within mitochondrial networks. Nat. Comm. *7*, 12886.

Mouw, J.K., Yui, Y., Damiano, L., Bainer, R.O., Lakins, J.N., Acerbi, I., Ou, G., Wijekoon, A.C., Levental, K.R., Gilbert, P.M., et al. (2014). Tissue mechanics modulate microRNA-dependent PTEN expression to regulate malignant progression. Nat. Med. *20*, 360–367.

Nakai, A., Suzuki, M., and Tanabe, M. (2000). Arrest of spermatogenesis in mice expressing an active heat shock transcription factor 1. EMBO J *19*, 1545–1554.

Nargund, A.M., Pellegrino, M.W., Fiorese, C.J., Baker, B.M., and Haynes, C.M. (2012). Mitochondrial import efficiency of ATFS-1 regulates mitochondrial UPR activation. Science *337*, 587–590.

Nehrke, K., and Melvin, J.E. (2002). The NHX family of Na+-H+ exchangers in Caenorhabditis elegans. J. Biol. Chem. *277*, 29036–29044.

Northcott, J.M., Dean, I.S., Mouw, J.K., and Weaver, V.M. (2018). Feeling stress: the mechanics of cancer progression and aggression. Front. Cell Dev. Biol. *6*, 17.

Oria, R., Wiegand, T., Escribano, J., Elosegui-Artola, A., Uriarte, J.J., Moreno-Pulido, C., Platzman, I., Delcanale, P., Albertazzi, L., Navajas, D., et al. (2017). Force loading explains spatial sensing of ligands by cells. Nature *552*, 219–224.

Östling, P., Björk, J.K., Roos-Mattjus, P., Mezger, V., and Sistonen, L. (2007). Heat shock factor 2 (HSF2) contributes to inducible expression of hsp genes through interplay with HSF1. J. Biol. Chem. *282*, 7077–7086.

Oudin, M.J., and Weaver, V.M. (2016). Physical and chemical gradients in the tumor microenvironment regulate tumor cell invasion, migration, and metastasis. Cold Spring Harb. Symp. Quant. Biol. *81*, 189–205.

Papalazarou, V., Zhang, T., Paul, N.R., Juin, A., Cantini, M., Maddocks, O.D.K., Salmeron-Sanchez, M., and Machesky, L.M. (2020). The creatine–phosphagen system is mechanoresponsive in pancreatic adenocarcinoma and fuels invasion and metastasis. Nat. Metab. *2*, 62–80.

Park, J.S., Burckhardt, C.J., Lazcano, R., Solis, L.M., Isogai, T., Li, L., Chen, C.S., Gao, B., Minna, J.D., Bachoo, R., et al. (2020). Mechanical regulation of glycolysis via cytoskeleton architecture. Nature *578*, 621–626.

Paszek, M.J., Zahir, N., Johnson, K.R., Lakins, J.N., Rozenberg, G.I., Gefen, A., Reinhart-King, C.A., Margulies, S.S., Dembo, M., Boettiger, D., et al. (2005). Tensional homeostasis and the malignant phenotype. Cancer Cell *8*, 241–254.

Paul, S., Ghosh, S., Mandal, S., Sau, S., and Pal, M. (2018). NRF2 transcriptionally activates the heat shock factor 1 promoter under oxidative stress and affects survival and migration potential of MCF7 cells. J. Biol. Chem. *293*, 19303–19316.

Perry, S.W., Norman, J.P., Barbieri, J., Brown, E.B., and Gelbard, H.A. (2011). Mitochondrial membrane potential probes and the proton gradient: a practical usage guide. BioTechniques *50*, 98–115.

Pouysségur, J., Sardet, C., Franchi, A., L'Allemain, G., and Paris, S. (1984). A specific mutation abolishing Na+/H+ antiport activity in hamster fibroblasts precludes growth at neutral and acidic pH. Proc. Natl. Acad. Sci. USA *81*, 4833–4837.

Quirós, P.M., Prado, M.A., Zamboni, N., D'Amico, D., Williams, R.W., Finley, D., Gygi, S.P., and Auwerx, J. (2017). Multi-omics analysis identifies ATF4 as a key regulator of the mitochondrial stress response in mammals. J. Cell Biol. *216*, 2027–2045.

Radisky, D.C., Levy, D.D., Littlepage, L.E., Liu, H., Nelson, C.M., Fata, J.E., Leake, D., Godden, E.L., Albertson, D.G., Nieto, M.A., et al. (2005). Rac1b and reactive oxygen species mediate MMP-3-induced EMT and genomic instability. Nature *436*, 123–127.

Reczek, C.R., and Chandel, N.S. (2017). The two faces of reactive oxygen species in cancer. Annu. Rev. Cancer Biol. *1*, 79–98.

Reczek, C.R., Birsoy, K., Kong, H., Martínez-Reyes, I., Wang, T., Gao, P., Sabatini, D.M., and Chandel, N.S. (2017). A CRISPR screen identifies a pathway required for paraquat-induced cell death. Nat. Chem. Biol. *13*, 1274–1279.

Reichmann, D., Voth, W., and Jakob, U. (2018). Maintaining a healthy proteome during oxidative stress. Mol. Cell *69*, 203–213.

Ristow, M. (2014). Unraveling the truth about antioxidants: mitohormesis explains ROS-induced health benefits. Nat. Med. *20*, 709–711.

Ristow, M., and Schmeisser, S. (2011). Extending life span by increasing oxidative stress. Free Radic. Biol. Med. *51*, 327–336.

Rossiter, N.J., Huggler, K.S., Adelmann, C.H., Keys, H.R., Soens, R.W., Sabatini, D.M., and Cantor, J.R. (2020). CRISPR screens in physiologic medium reveal conditionally essential genes in human cells. bioRxiv. https://doi.org/10.1101/2020.08.31.275107.

Royer, L.A., Weigert, M., Günther, U., Maghelli, N., Jug, F., Sbalzarini, I.F., and Myers, E.W. (2015). ClearVolume: open-source live 3D visualization for light-sheet microscopy. Nat. Methods *12*, 480–481.

Russell, W.K., Park, Z.Y., and Russell, D.H. (2001). Proteolysis in mixed organic-aqueous solvent systems: applications for peptide mass mapping using mass spectrometry. Anal. Chem. *73*, 2682–2685.

Samuel, M.S., Lopez, J.I., McGhee, E.J., Croft, D.R., Strachan, D., Timpson, P., Munro, J., Schröder, E., Zhou, J., Brunton, V.G., et al. (2011). Actomyosin-mediated cellular tension drives increased tissue stiffness and β-catenin activation to induce epidermal hyperplasia and tumor growth. Cancer Cell *19*, 776–791.

Santagata, S., Hu, R., Lin, N.U., Mendillo, M.L., Collins, L.C., Hankinson, S.E., Schnitt, S.J., Whitesell, L., Tamimi, R.M., Lindquist, S., and Ince, T.A. (2011). High levels of nuclear heat-shock factor 1 (HSF1) are associated with poor prognosis in breast cancer. Proc. Natl. Acad. Sci. USA *108*, 18378–18383.

Schafer, Z.T., Grassian, A.R., Song, L., Jiang, Z., Gerhart-Hines, Z., Irie, H.Y., Gao, S., Puigserver, P., and Brugge, J.S. (2009). Antioxidant and oncogene rescue of metabolic defects caused by loss of matrix attachment. Nature *461*, 109–113.

Schedin, P., and Keely, P.J. (2011). Mammary gland ECM remodeling, stiffness, and mechanosignaling in normal development and tumor progression. Cold Spring Harb. Perspect. Biol. *3*, a003228.

Scherz-Shouval, R., Santagata, S., Mendillo, M.L., Sholl, L.M., Ben-Aharon, I., Beck, A.H., Dias-Santagata, D., Koeva, M., Stemmer, S.M., Whitesell, L., and Lindquist, S. (2014). The reprogramming of tumor stroma by HSF1 is a potent enabler of malignancy. Cell *158*, 564–578.

Schmidt, O., Pfanner, N., and Meisinger, C. (2010). Mitochondrial protein import: from proteomics to functional mechanisms. Nat. Rev. Mol. Cell Biol. *11*, 655–667.

Schneider, H.C., Berthold, J., Bauer, M.F., Dietmeier, K., Guiard, B., Brunner, M., and Neupert, W. (1994). Mitochondrial Hsp70/MIM44 complex facilitates protein import. Nature *371*, 768–774.

Sciacovelli, M., Gonçalves, E., Johnson, T.I., Zecchini, V.R., da Costa, A.S.H., Gaude, E., Drubbel, A.V., Theobald, S.J., Abbo, S.R., Tran, M.G.B., et al. (2016). Fumarate is an epigenetic modifier that elicits epithelial-to-mesenchymal transition. Nature *537*, 544–547.

Scialò, F., Sriram, A., Fernández-Ayala, D., Gubina, N., Lõhmus, M., Nelson, G., Logan, A., Cooper, H.M., Navas, P., Enríquez, J.A., et al. (2016). Mitochondrial ROS produced via reverse electron transport extend animal lifespan. Cell Metab *23*, 725–734.

Sprenger, H.G., and Langer, T. (2019). The good and the bad of mitochondrial breakups. Trends Cell Biol *29*, 888–900.

Srinivasan, S.R., Cesa, L.C., Li, X., Julien, O., Zhuang, M., Shao, H., Chung, J., Maillard, I., Wells, J.A., Duckett, C.S., and Gestwicki, J.E. (2018). Heat shock protein 70 (Hsp70) suppresses RIP1-dependent apoptotic and necroptotic cascades. Mol. Cancer Res. *16*, 58–68.

Sun, N., Youle, R.J., and Finkel, T. (2016). The mitochondrial basis of aging. Mol. Cell *61*, 654–666.

Tharp, K.M., and Weaver, V.M. (2018). Modeling tissue polarity in context. J. Mol. Biol. *430*, 3613–3628.

Tharp, K.M., Kang, M.S., Timblin, G.A., Dempersmier, J., Dempsey, G.E., Zushin, P.-J.H., Benavides, J., Choi, C., Li, C.X., Jha, A.K., et al. (2018). Actomyosin-mediated tension orchestrates uncoupled respiration in adipose tissues. Cell Metab *27*, 602–615.e4.

Tominaga, T., and Barber, D.L. (1998). Na-H exchange acts downstream of RhoA to regulate integrin-induced cell adhesion and spreading. Mol. Biol. Cell *9*, 2287–2303.

Tominaga, T., Ishizaki, T., Narumiya, S., and Barber, D.L. (1998). p160ROCK mediates RhoA activation of Na-H exchange. EMBO J *17*, 4712–4722.

Twig, G., and Shirihai, O.S. (2011). The interplay between mitochondrial dynamics and mitophagy. Antioxid. Redox Signal. *14*, 1939–1951.

Urlinger, S., Baron, U., Thellmann, M., Hasan, M.T., Bujard, H., and Hillen, W. (2000). Exploring the sequence space for tetracycline-dependent transcriptional activators: novel mutations yield expanded range and sensitivity. Proc. Natl. Acad. Sci. USA *97*, 7963–7968.

Vyas, S., Zaganjor, E., and Haigis, M.C. (2016). Mitochondria and cancer. Cell *166*, 555–566.

Wallace, D.C. (2012). Mitochondria and cancer. Nat. Rev. Cancer *12*, 685–698.

Wang, Q., Zhang, M., Torres, G., Wu, S., Ouyang, C., Xie, Z., and Zou, M.H. (2017). Metformin suppresses diabetes-accelerated atherosclerosis via the inhibition of Drp1-mediated mitochondrial fission. Diabetes *66*, 193–205.

Werner, E., and Werb, Z. (2002). Integrins engage mitochondrial function for signal transduction by a mechanism dependent on Rho GTPases. J. Cell Biol. *158*, 357–368.

Wiedemann, N., and Pfanner, N. (2017). Mitochondrial machineries for protein import and assembly. Annu. Rev. Biochem. *86*, 685–714.

Wouters, O.Y., Ploeger, D.T.A., van Putten, S.M., and Bank, R.A. (2016). 3,4-Dihydroxy-l-phenylalanine as a novel covalent linker of extracellular matrix proteins to polyacrylamide hydrogels with a tunable stiffness. Tissue Eng. Part C Methods *22*, 91–101.

Yoneda, T., Benedetti, C., Urano, F., Clark, S.G., Harding, H.P., and Ron, D. (2004). Compartment-specific perturbation of protein handling activates genes encoding mitochondrial chaperones. J. Cell Sci. *117*, 4055–4066.

Youle, R.J., and van der Bliek, A.M. (2012). Mitochondrial fission, fusion, and stress. Science *337*, 1062–1065.

Yun, J., and Finkel, T. (2014). Mitohormesis. Cell Metab. *19*, 757–766.

Zhang, Y., Lanjuin, A., Chowdhury, S.R., Mistry, M., Silva-García, C.G., Weir, H.J., Lee, C.L., Escoubas, C.C., Tabakovic, E., and Mair, W.B. (2019). Neuronal TORC1 modulates longevity via AMPK and cell nonautonomous regulation of mitochondrial dynamics in C. elegans. eLife *8*, e49158.

Zhou, Y., Zhou, B., Pache, L., Chang, M., Khodabakhshi, A.H., Tanaseichuk, O., Benner, C., and Chanda, S.K. (2019). Metascape provides a biologist-oriented resource for the analysis of systems-level datasets. Nat. Commun. *10*, 1523.

Please cite this article in press as: Tharp et al., Adhesion-mediated mechanosignaling forces mitohormesis, Cell Metabolism (2021), https://doi.org/10.1016/j.cmet.2021.04.017

CellPress

STAR★METHODS

KEY RESOURCES TABLE

REAGENT or RESOURCE	SOURCE	IDENTIFIER
Antibodies		
Cleaved Caspase-3 (Asp175)	Cell Signaling	RRID: AB_2341188
HSF1	Cell Signaling	RRID: AB_2120258
SLC9A1	SCBT	RRID: AB_2191254
HSP60	SCBT	RRID: AB_783870
Total OxPhos WB Antibody Cocktail	Abcam	RRID: AB_2629281
YME1L1	Invitrogen	RRID: AB_2649732
HSP70	SCBT	RRID: AB_627759
mtHSP70	SCBT	RRID: AB_2120468
β-Actin	Sigma	RRID: AB_476744
FAK pY397	Invitrogen	RRID: AB_1500096
FAK	BD	RRID: AB_397495
pMLCK	Cell Signaling	RRID: AB_330248
Bacterial and virus strains		
Bespoke lentiviral particles with psPAX2 and pMD2.G	Addgene	12260 and 12259
Chemicals, peptides, and recombinant proteins		
3,4-Dihydroxy-L-phenylalanine (DOPA)	Alfa Aeser	A1131106
Human fibronectin	EMD Millipore	FC010
Paraformaldehyde	Electron Microscopy Services	15710
Rhod-2 AM	ThermoFisher	R1244
Calcium green-1 AM	Life Technologies	C3011MP
H2DCFDA	ThermoFisher	D399
MitoPy1	Tocris	4428
Fura-2 AM	Abcam	ab120873
TMRE	ThermoFisher	T669
BECEF	Invitrogen	B1150
Nigericin	Invitrogen	N1495
TRIzol	Invitrogen	15596-018
M-MLV reverse transcriptase	BioChain	Z5040002
Ribolock	ThermoFisher	EO0384
PerfeCTa SYBR Green FastMix	Quantabio	95072-05K
MitoPy1	Tocris	4428
Y-27632 (ROCK inhibitor)	Tocris	1254
Celastrol	Tocris	3203
KRIBB11	Selleckchem	S8402
MitoTempo	Cayman Chemical	16621
Ru360	MilliporeSigma	557440
SN-6	Tocris	2184
CGP 37157	Cayman Chemical	15611
BIX	Tocris	5512
EIPA	SigmaAldrich	A3085
Paraquat	MilliporeSigma	856177
Oligomycin A	MilliporeSigma	75351
FCCP	MilliporeSigma	C2920

(*Continued on next page*)

Please cite this article in press as: Tharp et al., Adhesion-mediated mechanosignaling forces mitohormesis, Cell Metabolism (2021), https://doi.org/10.1016/j.cmet.2021.04.017

Continued

REAGENT or RESOURCE	SOURCE	IDENTIFIER
Rotenone	MilliporeSigma	R8875
Antimycin A	MilliporeSigma	A8674
JC-9	ThermoFisher	D22421
MitoTracker Deep Red FM	ThermoFisher	M22426
MitoTracker Green FM	ThermoFisher	M7514
Peroxymycin	(Chung et al., 2018)	N/A
Critical commercial assays		
Pierce BCA Protein Assay Kit	ThermoFisher	23225
Deposited data		
RNAseq (Related to Figure 4B)	GEO	GEO: GSE171076
Experimental models: Cell lines		
HEK293T	ATCC	N/A
MCF10A (36 year old, Caucasian, female)	ATCC	N/A
MB-MDA-231 (51 year old, Caucasian, female)	ATCC	N/A
Experimental models: Organisms/strains		
FVB/N-Tg-MMTV-PyMT mice	The Jackson Laboratory	002374
C. elegans: Bristol (N2) strain as wild type (WT)	CGC	N/A
C. elegans: AGD710: N2, uthIs235 [sur-5p::hsf-1, myo-2p::tdTomato]	Dillin Lab	(Baird et al., 2014)
C. elegans: AGD2319: N2; unc-119(ed3) III; uthSi62[vha-6p::MLS::mRuby::unc-54 3'UTR, cb-unc-119(+)] IV;	Dillin Lab	This study
C. elegans: AGD2490: N2; uthIs235 [sur-5p::hsf-1, myo-2p::tdTomato]; dvIs19[pAF15(gst-4p::GFP::NLS)]	Dillin Lab	This study
C. elegans: CL2166: N2; gst-4p::GFP	CGC	(Baird et al., 2014)
C. elegans: SJ4100: N2; zcIs13(hsp-6p::GFP)	CGC	(Yoneda et al., 2004)
Oligonucleotides		
Random hexamers	Roche	11034731001
qPCR primers, see list in qPCR section	This paper	N/A
shRNA HSF1-1 TRCN0000007481 (HSF1): 5'CCGGGCAGGTTGTTCAT AGTCAGAACTCGAGTTCTGACTAT GAACAACCTGCTTTTT	Dillin lab and Sigma	TRCN0000007481
shRNA HSF1-2 TRCN0000318652 (HSF1): 5'CCGGGCACATTCCATG CCCAAGTATCTCGAGATACTTGG GCATGGAATGTGCTTTTT	Dillin lab and Sigma	TRCN0000318652
shRNA HSF1-1 TRCN0000007481 (HSF1): 5'CCGGGCAGGTTGTTCA TAGTCAGAACTCGAGTTCTGACT ATGAACAACCTGCTTTTT	Dillin lab	N/A
shRNA HSF1-2 TRCN0000318652 (HSF1): 5'CCGGGCACATTCCATG CCCAAGTATCTCGAGATACTTGG GCATGGAATGTGCTTTTT	Dillin lab	N/A
sgRNA YME1L1 1: 5'-TTCCG TTTCTGGGAGGAGTG	This paper	N/A

(*Continued on next page*)

Please cite this article in press as: Tharp et al., Adhesion-mediated mechanosignaling forces mitohormesis, Cell Metabolism (2021), https://doi.org/10.1016/j.cmet.2021.04.017

Continued

REAGENT or RESOURCE	SOURCE	IDENTIFIER
sgRNA YME1L1 2: 5'-GCAGTAGCTGTAGGAAGGGG, and	This paper	N/A
sgRNA YME1L1 3: CTCCTCCCAGAAACGGAAAA-5'	This paper	N/A
Recombinant DNA		
V737N β1 integrin, see associated section of STAR Methods for sequence	(Paszek et al., 2005)	N/A
β1 integrin, see associated section of STAR Methods for sequence	(Paszek et al., 2005)	N/A
MTS-roGFP2, see associated section of STAR Methods for sequence	This study	N/A
ROCK:ER	(Croft and Olson, 2006)	N/A
vha-6p::MLS::mRuby (C. elegans) ATGTTGTCCAAACGCATTGTTACC GCTCTTAACACCGCCGTCAAGGT CCAAAATGCCGGAATCGCCAC CACCGCCCGCGGA	Dillin lab	N/A
Constitutively active HSF1, see associated section of STAR methods for sequence	Dillin lab	N/A
Software and algorithms		
RNA STAR	(Dobin et al., 2013)	https://github.com/alexdobin/STAR
HOMER	(Lin et al., 2010)	http://homer.ucsd.edu/homer/ngs/rnaseq/index.html
Cluster	(Eisen et al., 1998)	http://bonsai.hgc.jp/~mdehoon/software/cluster/software.htm
Java TreeView	N/A	http://jtreeview.sourceforge.net/
Metascape	(Zhou et al., 2019)	https://metascape.org
Seahorse Wave	Agilent	N/A
MaxQuant	(Cox and Mann, 2008)	https://www.maxquant.org/
artMS	http://artms.org	http://bioconductor.org/packages/release/bioc/html/artMS.html
MSstats	(Choi et al., 2014)	https://www.bioconductor.org/packages/release/bioc/html/MSstats.html
FIJI-ImageJ 1.53+	NIH	https://imagej.net/Fiji
MitoMAPR	(Zhang et al., 2019)	N/A
FracLac	NIH	https://imagej.nih.gov/ij/plugins/fraclac/FLHelp/Introduction.htm
Other		
KAPA RNA HyperPrep Kit	Roche	KK8540

RESOURCE AVAILABILITY

Lead contact

Further information and requests for resources and reagents should be directed to and will be fulfilled by the Lead Contact, Valerie M. Weaver (Valerie.Weaver@ucsf.edu).

Materials availability

Cell lines, animal models, and expression vectors used in this manuscript are available from the lead contact upon request.

Data and code availability

The accession number for the RNA sequencing data reported in this paper is GEO:GSE171076. https://www.ncbi.nlm.nih.gov/geo/query/acc.cgi?acc=GSE171076

Please cite this article in press as: Tharp et al., Adhesion-mediated mechanosignaling forces mitohormesis, Cell Metabolism (2021), https://doi.org/10.1016/j.cmet.2021.04.017

EXPERIMENTAL MODEL AND SUBJECT DETAILS

Human cell culture

MCF10A and MB-MDA-231 cells were sourced from ATCC, routinely tested and found to be free of mycoplasma contamination, and maintained below passage 22. All cells were maintained and in 5% CO^2 at 37 °C. MCF10A were cultured in [5 mM] glucose DMEM:F12 (1:1 mixture of F:12 [10mM] glucose and [0 mM] glucose DMEM) (Life Technologies, 11765054 and 11966025) supplemented with 5% Horse Serum (Gibco, 16050-122), 20 ng/mL epidermal growth factor (Peprotech), 10 μg/mL insulin (Sigma), 0.5 μg/mL hydrocortisone (Sigma), 100 ng/mL cholera toxin (Sigma, C8052-2MG), and 1x penicillin/streptomycin (Gibco). MB-MDA-231 tumor cells (ATCC) were grown in 5 mM glucose DMEM supplemented with 10% fetal bovine serum (FBS) (Hyclone) and 1x penicillin/streptomycin. HEK293T cells (ATCC) were maintained in DMEM supplemented with 10% FBS and 1x penicillin/streptomycin and were used to produce lentiviral particles with psPAX2 (Addgene 12260), pMD2.G (Addgene 12259) and various transfer vectors described hereafter (https://www.addgene.org/guides/lentivirus/).

Murine mammary tumor model

FVB/N-Tg-MMTV-PyMT mice (The Jackson Laboratory) were treated with BAPN (3 mg per kg body weight; Spectrum) in the drinking water (n = 6 per group) injected intraperitoneally twice per week. Treatment started at 4 weeks and mice were tissues were harvested at 11 weeks of age. Mammary tumors were excised and fixed in 4% paraformaldehyde, cryosectioned, and immunostained for microscopy.

C. elegans strains and maintenance

All *C. elegans* strains are derivatives of the Bristol N2 strain from Caenorhabditis Genetics Center (CGC) and are listed below. All worms are maintained at 15 °C on standard nematode growth media (NGM) plates and fed OP50 *E. coli* B bacteria and are maintained for a maximum of 20-25 generations (weeks). For all experiments, worms are synchronized using a standard bleaching protocol by degrading carcasses with bleach solution (1.8% sodium hypochlorite, 0.375M KOH), then washing eggs four times with M9 solution (22 mM KH_2PO_4 monobasic, 42.3 mM Na_2HPO_4, 85.6 mM NaCl, 1 mM $MgSO_4$), followed by L1 arresting synchronization, achieved by floating eggs in M9 overnight in a 20 °C incubator on a rotator for a maximum of 16 hours. L1s are plated on RNAi bacteria (NGM + 1 μM IPTG and 100 μg/mL carbenicillin; HT115 *E. coli* K strain containing pL4440 vector control or pL4440 with RNAi of interest) until the desired stages of adulthood. All RNAi constructs were isolated from the Vidal library and verified sequences are available below.

hsf-1

CGTCAGCGCGCCCGTACCGGCACATCAAATCCATTTTCCGGGTACTGTTGCTCATTATCAAACAACAAATCCTCGGCTCCATCAT
AATTCGACGTCTCCGGAGCATTTTCAAGAGCAAGCTGTCTGAGTGGATCCTCGGATCCTTCTTCATCATCATCCAACGGTACATTA
TTCCCAAAATCATCCCAATTATGATTACTGACTAAATCTCTGAAACTCTCCAATGAAGTATCAGTTCCAGTGAAATATTCTTGAAGTT
CTTGAGATAATTGACGATCAAATGATGGAGAGAGTCCGAGAGTTGGAGAATATAGATTTTGATGAGGATCTGCGTTGGTGGATGAG
GTGGAAGTCGTTGGATGATGCTGATCTTCTATTGCCATTAGCTTCTGATGCGGTTGAAGGTATTGATGAGATGGTTGATATGGAAT
CATTGAAGGATCTGAAGGCATGAAGCCACTGTAATTGTTCACAAATCCTCCCGAATAGTCTTGTTGCGGCTGAAAATTTCG
AATTTTTAGAC

nhx-2

GTCAACGAAGTTCTTTTTATTGCCGTGTTCGGAGAATCTCTATTGAACGACGGAGTTGCTGTTGTACTTTATCGAATGTTCTTGACCT
TCTCTGAAATTGGAACTGAGAATCTGATAACATCTGATTATATCAATGGAGGTGTTTCTTTCCTGGTTGTTGCATTTGGTGGAATTGG
AATTGGTCTTCTTTTTGCATTTTTGACAAGTCTTGTTACAAGATTTGCTAGAGATGAAGAGGTCAAAGTGCTCAATTCTGTATTTATTC
TCATTCTTCCGTACACTTGTTATCTTTGTGGAGAACTTTTCGGTCTTTCAAGTATTATGGC

ina-1

AACATCAAATGGATACGTTTCAAATGTCGGCGAAAAGGATTATCTGGACTTGACATTCACTGTGGAAAACAAGAAAGAAAAGGCTTA
TCAAGCGAATTTTTATCTAGAATATAATGAAGAAGAGCTTGAACTTCCACAAGTTCAAGGTTCCAAGAGAATGATTGCTGAAACAATT
GGAAAGAATATTGTGCATTTGCCACTTGGAAATCCAATGAATGGAGCATCAAAACATCAATTTACGATCCAATTCAAATTGACTCGT
GGAAGAACTGAAGGAATTGGAAAGGCACTCAAATTCATGGCACATGTCAATTCCACGTCACAAGAAACCGAGGAAGAGTTGAAAG
ATAATAAATGGGAAGCTGAAGTTCAGATTATCAAGAAGGCAGAGCTGGAGATCTATGGAATCAGTGACCCTGATAGAGTATTCTTT
GGAGGAAAAGCAAGAGCAGAGTCTGAATTGGAATTGGAAGAAGATATTGGAACAATGGTTAGACATAACTATACAATTATTAATCAT
GGTCCATGGACTGTTCGAAATGTGGAAGCACACATTTCTTGGCCTTATCAACTCCGTTCTAGGTTTGGAAGAGGAAAGAATGCTCT
CTATCTATTGGATGTACCGACTATTACAACAGAATTCACAGATGGAACAAGTGAAGTTAGAAAGTGTTTCATCAAACAACAGTACGA
ATATGTGAATCCTGCAGAAATTAAATTGAACACTAAATATAGTACTCAAGAGACTGCTCCACATCGGGTAGAGCATAGAATGAAAA
GAGAAATTGATGAGGATGAGGAAGAACAATCAGATGATCTAGGAGCCGTGGAAGAGAATATTCCTTGGTTCTCAACAGCTAATTTC
TGGAATCTTTTTGCAATTAAAGGAGGTGATGGACG

pat-3

GATATGGTTTGTGGAGTTTGTCGATGCAAAGGAGGAAATGTTGGAAAATATTGTGAATGTAATAGACCTGGAATGAGTACTGCTGC
GCTCAATGAAAAATGCAAAAGAACTAACGAATCAGCAATCTGTGAGGGTCGTGGTGTGTGTAACTGTGGACGTTGTGAATGTAATC
CACGTGCCAATCCAGAAGAACAAATCTCTGGAGAATTCTGTGAATGCGACAACTTCAATTGCCCACGACACGATCGTAAAATCTGT
GCAGAACACGGTGAATGCAACTGTGGAAAGTGTATTTGTGCACCTGGATGGACTGGAAGAGCCTGTGAATGCCCAATTTCAACT

Please cite this article in press as: Tharp et al., Adhesion-mediated mechanosignaling forces mitohormesis, Cell Metabolism (2021), https://doi.org/10.1016/j.cmet.2021.04.017

GATTCATGCCTCTCTGCAAATGGAAAAATCTGTAATGGAAAGGGTGAATGTATTTGTGGAAGATGTCGATGCTTCGATTCGCCCGA
CGGAAATCGATATTCGGGAGCGAAATGCGAAATTTGTCCGACGTGTCCGACGAAATGTGTGGAATACAAGAATTGTGTAATGTGC
CAGCAATGGCAGACAGGGCCACTTAATGAGACCGCCTGTGATCAGTGTGAATTCAAAGTTATTCCTGTTGAGGAATTACCCAATC
TCAACGAAACTACACCCTGCCAATTTGTGGATCCAGCTGATGATTGTACATTCTATTATCTCTACTATTACGATGAGGCCACAGATA
ATGCAACAGTCTGGGTCAGAAAACATAAAGATTGTCCTCCACCTGTCCCTGTGCTCGCAATTGTGCTCGGAGTCATTGCGGGTAT
CGTAATCCTCGGAATTCTTCTCTTGTTGCT

skn-1

TGTACACGGACAGCAATAATAGGAGCTTTGATGAAGTCAACCATCAGCATCAACAAGAACAAGATTTCAATGGCCAATCCAAATAT
GATTATCCACAATTCAACCGTCCAATGGGTCTCCGTTGGCGTGATGATCAACGGATGATGGAGTATTTCATGTCGAATGGTCCAGT
AGAAACTGTTCCAGTTATGCCAATACTCACCGAGCATCCACCAGCATCTCCATTCGGTAGAGGACCATCTACAGAACGTCCAACC
ACATCATCTCGATACGAGTACAGTTCGCCTTCTCTCGAGGATATCGACTTGATTGATGTGCTATGGAGAAGTGATATTGCTGGAGA
GAAGGGCACACGACAAGTGGCTCCTGCTGATCAGTACGAATGTGATTTGCAGACGTTGACAGAGAAATCGACAGTAGCG

ymel-1

TCGATTCAGTTGGCTCAAAACGTGTTTCGAATTCCATCCATCCATATGCAAATCAAACGATTAATCAACTTCTCAGGTAACAATTTG
CTCAATTTTGTGCATTAAAAACTCATCTCCTGATGTTTTCAGTGAAATGGATGGCTTCACCCGTAACGAGGGAATCATTGTAATTGC
CGCAACAAATCGTGTCGACGACCTC

METHOD DETAILS

ECM coated polyacrylamide hydrogel cell culture surfaces (PA-gels)

Cleaned (10% ClO, 1M HCL, then 100% EtOH) round #1 German glass coverslips (Electron Microscopy Services) were coated with 0.5% v/v (3-Aminopropyl)triethoxysilane (APTES, Sigma, 440140), 99.2% v/v ethanol, and 0.3% v/v glacial acetic acid for 2 h and then cleaned in 100% EtOH on an orbital shaker at 22 °C. APTES activated coverslips were coated with PBS buffered acrylamide / bis-acrylamide (Bio-Rad, 1610140 and 1610142) solutions (3% / 0.05% for 400 Pa, 7.5% / 0.07% for 6k Pa, and 10% / 0.5% for 60k Pa) polymerized with TEMED (0.1% v/v) (Bio-Rad, 1610801) and Potassium Persulfate (0.1% w/v) (Fisher, BP180) to yield a final thickness of ~ 85 μm. PA-gels were washed with 70% EtOH and sterile PBS prior 3,4-dihydroxy-L-phenylalanine (DOPA, CAS 59-92-7, Alfa Aeser, A1131106) coating for 5 min at 22 °C protected from light with sterile filtered DOPA in pH 10 [10 mM] Tris buffer (Wouters et al., 2016). DOPA coated PA-gels were washed 2x with sterile PBS and ECM functionalized with 5 μg/mL human fibronectin (Millipore, FC010) in sterile PBS 1 h at 37 °C to generate an expected fibronectin coating density of 6 $\mu M/cm^2$.

Immunofluorescence microscopy

Cells or tissues were fixed in 4% paraformaldehyde (Electron Microscopy Services, 15710) in 1X PBS for 30 min at room temperature, washed and blocked with a blocking buffer (HBSS fortified with: 10% FBS (Hyclone), 0.1% BSA (Fischer, BP1600), 0.05% saponin (EMD Millipore, L3771), and 0.1% Tween 20 (Fischer, BP337500). Primary antibodies [1:100-1:200] for 2 h at RT or 24 h at 4 °C, Secondary antibodies [1:1000] for 2 h at 22 °C. Samples were imaged with a Nikon Eclipse Ti spinning disc microscope, Yokogawa CSU-X, Andor Zyla sCMOS, Andor Multi-Port Laser unit, and Molecular Devices MetaMorph imaging suite.

Antibodies used: Cleaved Caspase-3 (Asp175) (Cell Signaling, 9661, AB_2341188), HSF1 (Cell Signaling, 4356, AB_2120258), SLC9A1 (sc-136239, AB_2191254), and HSP60 (LK1, sc-59567, AB_783870).

MitoTacker staining

Mitotracker deep red FM or Mitotracker Green FM (Invitrogen, M22426 and M7514) was solubilized in DMSO to yield 100 μM frozen aliquots which were diluted into media to yield a 10 μM stock which was added directly to cell culture media already in the culture yielding a final concertation of 100 nM (to prevent media change derived fluid flow shear stress) 30 min before 4% PFA fixation or live cell imaging (MitoTracker red FM was used for PFA fixed samples). Three to five images per condition were analyzed using MitoMAPR (Zhang et al., 2019) to describe junctions per network (presented in the figure legend).

TMRE, H2DCFDA, Rhod-2 AM, Fura-2 AM, Calcium Green-1 AM, and MitoPy1

Stained cells were washed twice with PBS and imaged on a SpectraMax i5 Multi-Mode plate reader. Experiments were carried out with 50k or 100k cells per well in 500 μL of media in 24 well format with or without fibronectin coated PA-gels (indicated). 2 μM Rhod-2 AM (Thermo, R1244) and 2 μM Calcium green-1 AM (Life Technologies, C3011MP) was added to culture media and allowed to stain at 22 °C for 20 min prior to imaging (frozen Rhod-2 AM aliquots were used only when the DMSO suspension remained clear), or 2 μM H_2DCFDA (Thermo, D399) was added to media 1 or 4 h prior to imaging, 5 μM MitoPy1 (Tocris, 4428), or 1 μM Fura-2 AM (ab120873), or 2 nM TMRE (Fischer, T669) was applied to cells in media without disturbing the existing culture media (similar dilution scheme to MitoTracker) for 1 h prior to microscopy or plate reader assay.

Intracellular pH (pH_i)

10 μM BECEF (Invitrogen, B1150) was added to cell culture media for 30 min at 37 °C in 5 % CO_2 incubator. Cultures were washed twice and then fluorescent intensities of BCECF was determined with a SpectraMax i5 plate reader in a buffer comprised of 25 mM HEPES, 140 mM NaCl, 5 mM KCl, 1 mM $KHPO_4$, 1 mM $MgSO_4$, 2 mM $CaCl_2$, and 5 or 25 mM glucose. The cultures were then treated

Please cite this article in press as: Tharp et al., Adhesion-mediated mechanosignaling forces mitohormesis, Cell Metabolism (2021), https://doi.org/10.1016/j.cmet.2021.04.017

with a pH 7.7 buffer containing 10 μM Nigericin (Invitrogen, N1495), 25 mM HEPES, 105 mM KCl, and 1 mM MgCl for 5 min at 22 °C followed by determination of BCECF fluorescent intensities at high pH. The cultures were then treated with a pH 6.6 buffer containing 10 μM Nigericin (Invitrogen, N1495), 25 mM HEPES, 105 mM KCl, and 1 mM MgCl for 5 min at 22 °C followed by determination of BCECF fluorescent intensities at low pH. A linear relationship between pH 6.6 and 7.7 was observed and sample pH was estimated relative to pH standards for each individual culture well.

qPCR

Total RNA was isolated from biological samples with TRIzol (Invitrogen, 15596-018) according to the manufacturer's instructions. cDNA was synthesized with 1 μg total RNA in 10 μL reaction volume with RNA using M-MLV reverse transcriptase (BioChain, Z5040002-100K) and 5X reaction buffer (BioChain, Z5040002-100K), random hexamers (Roche, 11034731001), dNTPs, and 1U of Ribolock (ThermoFischer, EO0384). RT-thermocycler program: random hexamers and RNA incubated at 70°C for 10 min, then held at 4 °C until the addition of the M-MLV reverse transcriptase, dNTPs, Ribolock, and M-MLV-reverse transcriptase, then 50 °C for 1 h, 95 °C for 5 min, then stored at -20 °C until qPCR was performed. The reverse transcription reaction was then diluted to 50 μL total volume with ddH_2O rendering a concentration of 20 ng RNA per 1 μL used in subsequent qPCR reactions. qPCR was performed in triplicate using PerfeCTa SYBR Green FastMix (Quantabio, 95072-05K) with an Eppendorf Mastercycler RealPlex^2. qPCR thermocycler program: 95 °C for 10 min, then 40 cycles of a 95 °C for 15 s, 60 °C for 20 s, followed by a melt curve 60-95 °C over 10 min. Melt curves and gel electrophoresis were used to validate the quality of amplified products. The ΔCt values from independent experiments were used to calculate fold change of expression using the $2^{-\Delta\Delta Ct}$ method. For each gene measured, the SEM of the ΔCt values was calculated and used to generate positive and negative error values in the $2^{-\Delta\Delta Ct}$ fold change space. Plots of qPCR data display bars representing the mean fold change ±SEM and individual points representing the fold change value for each experiment relative to the mean.

qPCR primers used:

5'-Forward		
UCP2	GGTGGTCGGAGATACCAAAG	
NRF2	CGGTATGCAACAGGACATTG	
18S	GGACACGGACAGGATTGACA	
YME1L1 CCCATGTCTCTGCACAATCC		ACCCCTTCACGAATGATGG
PKM1	CTATCCTCTGGAGGCTGTGC	
PKM2	CCACTTGCAATTATTTGAGGAA	
TFAM	AAGATTCCAAGAAGCTAAGGGTGA	CAGAGTCAGACAGATTTTTCCAGTTT
HNRNPA1 CCTTTGACGACCATGACTCC		ACGACCGAAGTTGTCATTCC
ATF5	CTGGCTCCCTATGAGGTCCTTG	
HSPD1 GATGCTGTGGCCGTTACAATG		GTCAATTGACTTTGCAACAGTCACAC
HSPA9 CAAGCGACAGGCTGTCACCAAC		CAACCCAGGCATCACCATTGG
HSPE1 TGGCAGGACAAGCGTTTAG		GGTTACAGTTTCAGCAGCAC
LONP1 CATTGCCTTGAACCCTCTC		ATGTCGCTCAGGTAGATGG
HSF1 GCCTTCCTGACCAAGCTGT		
XBP1sp TGCTGAGTCCGCAGCAGGTG		GCTGGCAGGCTCTGGGGAAG
CHOP	GCACCTCCCAGAGCCCTCACTCTCC	GTCTACTCCAAGCCTTCCCCCTGCG
GAPDH CGACCACTTTGTCAAGCTCA		AGGGGAGATTCA GTGTGGTG
LOX	GAACCAGGTAGCTGGGGTTT	

Western blotting

Cells were freeze-thaw lysed (-80 °C) with RIPA buffer (150 mM NaCl, 1% v/v NP-40, 0.5% w/v sodium deoxycholate, 0.1% w/v SDS, and 25 mM tris) containing protease and phosphatase inhibitor coctail (GenDepot, P3100 and P3200). Protein content was determined via BCA (Pierce, 23225) and 5-10 μg of protein was mixed with 5x Laemmli buffer to generate final 1x concentration (50 mM Tris-HCl (Fischer, AAJ2267636) pH 6.8, 4% w/v SDS (Sigma, L3771), 10% v/v glycerol (Fischer, BP229-1), 0.1% w/v bromophenol blue (Bio-Rad, 1610404), 2% v/v β-mercaptoethanol (Bio-Rad, 1610710) and heated to 95 °C for 5 min (no heating of the samples used for the total oxphos (abcam, ab110413) blots). 10%-gels (Bio-Rad, Bulletin_6201) were cast in a PROTEAN Plus multi casting chamer (Bio-Rad). Samples were loaded (~20 μL) and run to completion in Tris Glycine SDS running buffer (25 mM Tris, 192 mM glycine (Fischer, BP381), and 0.1% SDS, pH ~8.6), wet transferred @ 100V for 60 min to methanol (Fischer, A412) activated PVDF (BioRad, 1620177) in Towbin transfer buffer containing (25 mM Tris, 192 mM Glycine, 20% v/v methanol, pH ~8.3). Protein loaded

Please cite this article in press as: Tharp et al., Adhesion-mediated mechanosignaling forces mitohormesis, Cell Metabolism (2021), https://doi.org/10.1016/j.cmet.2021.04.017

PVDF membranes were washed 2x with TBST (20 mM tris, 150 mM NaCl (S271), 0.1% w/v Tween20) and blocked in 5% milk TBST buffer for 1 h at 22 °C on an orbital shaker.

Antibodies used: HSF1 (Cell Signaling, HSF1, 4356, AB_2120258), YME1L1 (Invitrogen, PA564299, AB_2649732) HSP60 (LK1, sc-59567, AB_783870), HSP70 (3A3, sc32239, AB_627759), mtHSP70 (D-9, sc-133137, AB_2120468), Total OXPHOS WB Antibody Cocktail (Abcam, ab110413, AB_2629281), β-Actin (Sigma, A5441, AB_476744), FAK pY397 (Invitrogen, 44-625G, AB_1500096), FAK (BD, 610088, AB_397495), and pMLCK (Cell Signaling, 3671, AB_330248).

MTS-roGFP2

ATGCTTGCCACTAGAGTCTTTTCATTGGTAGGTAAAAGGGCCATAAGTACATCAGTCTGCGTGAGAGCCCACACCGGACCGGTCA
GCAAGGGCGAGGAGCTGTTCACCGGGGTGGTGCCCATCCTGGTCGAGCTGGACGGCGACGTAAACGGCCACAAGTTCAGCGT
GTCCGGCGAGGGCGAGGGCGATGCCACCTACGGCAAGCTGACCCTGAAGTTCATCAGCACCACCGGCAAGCTGCCCGTGCCC
TGGCCCACCCTCGTGACCACCCTGACCTACGGCGTGCAGTGCTTCAGCCGCTACCCCGACCACATGAAGCGGCACGACTTCTT
CAAGTCCGCCATGCCCGAAGGCTACGTCCAGGAGCGCACCATCTTCTTCAAGGACGACGGCAACTACAAGACCCGCGCCGAGG
TGAAGTTCGAGGGCGACACCCTGGTGAACCGCATCGAGCTGAAGGGCATCGACTTCAAGGAGGACGGCAACATCCTGGGGCAC
AAGCTGGAGTACAACTACAACTGCCACAACGTCTATATCATGGCCGACAAGCAGAAGAACGGCATCAAGGTGAACTTCAAGATCC
GCCACAACATCGAGGACGGCAGCGTGCAGCTCGCCGACCACTACCAGCAGAACACCCCCATCGGCGACGGCCCCGTGCTGCT
GCCCGACAACCACTACCTGAGCACCTGCTCCGCCCTGAGCAAAGACCCCAACGAGAAGCGCGATCACATGGTCCTGCTGGAGT
TCGTGACCGCCGCCGGGATCACTCTCGGCATGGACGAGCTGTACAAGTAA

V737N β1 integrin

Weaver lab generated (Dr. Jonathan Lakins) puromycin lentiviral transfer vector expressing 3x myc tagged V737N β1 integrin using the tetracycline rtTA2(S)-M2 (Urlinger et al., 2000) inducible promoter for 24 h with doxycycline [200 ng/mL] (Sigma, D9891). No respiratory repression of MCF10A or MB-MDA-231 cells was observed with 200 ng/mL, 1 μg/mL, or 2 μg/mL doxycycline. Previous studies have demonstrated that 24 h of 30 μg/mL doxycycline treatment can suppress mitochondrial respiration (Quirós et al., 2017).

ATGAATTTACAACCAATTTTCTGGATTGGACTGATCAGTTCAGTTTGCTGTGTGTTTGCTCAAACAGATGGCGAGCAGAAGCTGA
TCAGCGAGGAGGACCTGGGCGAGCAGAAGCTGATCAGCGAGGAGGACCTGGGCGAGCAGAAGCTGATCAGCGAGGAGGACC
TGGGCGGCGCCCAAACAGATGAAAATCGATGTTTAAAAGCAAATGCCAAATCATGTGGAGAATGTATACAAGCAGGGCCAAATTG
TGGGTGGTGCACAAATTCAACATTTTTACAGGAAGGAATGCCTACTTCTGCACGATGTGATGATTTAGAAGCCTTAAAAAAGAAGG
GTTGCCCTCCAGATGACATAGAAAATCCCAGAGGCTCCAAAGATATAAAGAAAAATAAAAATGTAACCAACCGTAGCAAAGGAACA
GCAGAGAAGCTCAAGCCAGAGGATATTACTCAGATCCAACCACAGCAGTTGGTTTTGCGATTAAGATCAGGGGAGCCACAGACAT
TTACATTAAAATTCAAGAGAGCTGAAGACTATCCCATTGACCTCTACTACCTTATGGACCTGTCTTACTCAATGAAAGACGATTTGG
AGAATGTAAAAAGTCTTGGAACAGATCTGATGAATGAAATGAGGAGGATTACTTCGGACTTCAGAATTGGATTTGGCTCATTTGTGG
AAAAGACTGTGATGCCTTACATTAGCACAACACCAGCTAAGCTCAGGAACCCTTGCACAAGTGAACAGAACTGCACCAGCCCATT
TAGCTACAAAAATGTGCTCAGTCTTACTAATAAAGGAGAAGTATTTAATGAACTTGTTGGAAAACAGCGCATATCTGGAAATTTGGA
TTCTCCAGAAGGTGGTTTCGATGCCATCATGCAAGTTGCAGTTTGTGGATCACTGATTGGCTGGAGGAATGTTACACGGCTGCTG
GTGTTTTCCACAGATGCCGGGTTTCACTTTGCTGGAGATGGGAAACTTGGTGGCATTGTTTTACCAAATGATGGACAATGTCACCT
GGAAAATAATATGTACACAATGAGCCATTATTATGATTATCCTTCTATTGCTCACCTTGTCCAGAAACTGAGTGAAAATAATATTCAG
ACAATTTTTGCAGTTACTGAAGAATTTCAGCCTGTTTACAAGGAGCTGAAAAACTTGATCCCTAAGTCAGCAGTAGGAACATTATCT
GCAAATTCTAGCAATGTAATTCAGTTGATCATTGATGCATACAATTCCCTTTCCTCAGAAGTCATTTTGGAAAACGGCAAATTGTCAG
AAGGAGTAACAATAAGTTACAAATCTTACTGCAAGAACGGGGTGAATGGAACAGGGGAAAATGGAAGAAAATGTTCCAATATTTCC
ATTGGAGATGAGGTTCAATTTGAAATTAGCATAACTTCAAATAAGTGTCCAAAAAAGGATTCTGACAGCTTTAAAATTAGGCCTCTG
GGCTTTACGGAGGAAGTAGAGGTTATTCTTCAGTACATCTGTGAATGTGAATGCCAAAGCGAAGGCATCCCTGAAAGTCCCAAGT
GTCATGAAGGAAATGGGACATTTGAGTGTGGCGCGTGCAGGTGCAATGAAGGGCGTGTTGGTAGACATTGTGAATGCAGCACAG
ATGAAGTTAACAGTGAAGACATGGATGCTTACTGCAGGAAAGAAAACAGTTCAGAAATCTGCAGTAACAATGGAGAGTGCGTCTG
CGGACAGTGTGTTTGTAGGAAGAGGGATAATACAAATGAAATTTATTCTGGCAAATTCTGCGAGTGTGATAATTTCAACTGTGATAG
ATCCAATGGCTTAATTTGTGGAGGAAATGGTGTTTGCAAGTGTCGTGTGTGTGAGTGCAACCCCAACTACACTGGCAGTGCATGTG
ACTGTTCTTTGGATACTAGTACTTGTGAAGCCAGCAACGGACAGATCTGCAATGGCCGGGGCATCTGCGAGTGTGGTGTCTGTAA
GTGTACAGATCCGAAGTTTCAAGGGCAAACGTGTGAGATGTGTCAGACCTGCCTTGGTGTCTGTGCTGAGCATAAAGAATGTGTT
CAGTGCAGAGCCTTCAATAAAGGAGAAAAGAAAGACACATGCACACAGGAATGTTCCTATTTTAACATTACCAAGGTAGAAAGTCG
GGACAAATTACCCCAGCCGGTCCAACCTGATCCTGTGTCCCATTGTAAGGAGAAGGATGTTGACGACTGTTGGTTCTATTTTACGT
ATTCAGTGAATGGGAACAACGAGGTCATGGTTCATGTTGTGGAGAATCCAGAGTGTCCCACTGGTCCAGACATCATTCCAATTGTA
GCTGGTGTT**AAC**GCTGGAATTGTTCTTATTGGCCTTGCATTACTGCTGATATGGAAGCTTTTAATGATAATTCATGACAGAAGGGAG
TTTGCTAAATTTGAAAAGGAGAAAATGAATGCCAAATGGGACACGGGTGAAAATCCTATTTATAAGAGTGCCGTAACAACTGTGGT
CAATCCGAAGTATGAGGGAAAATGA

WT β1 integrin

Weaver lab generated (Dr. Jonathan Lakins) puromycin lentiviral transfer vector expressing 3× myc tagged β1 integrin using the tetracycline rtTA2(S)-M2 (Urlinger et al., 2000) inducible promoter for 24 h with doxycycline [200 ng/mL] (Sigma, D9891).

Please cite this article in press as: Tharp et al., Adhesion-mediated mechanosignaling forces mitohormesis, Cell Metabolism (2021), https://doi.org/10.1016/j.cmet.2021.04.017

ATGAATTTACAACCAATTTTCTGGATTGGACTGATCAGTTCAGTTTGCTGTGTGTTTGCTCAAACAGATGGCGAGCAGAAGCTGA
TCAGCGAGGAGGACCTGGGCGAGCAGAAGCTGATCAGCGAGGAGGACCTGGGCGAGCAGAAGCTGATCAGCGAGGAGGACC
TGGGCGGCGCCCAAACAGATGAAAATCGATGTTTAAAAGCAAATGCCAAATCATGTGGAGAATGTATACAAGCAGGGCCAAATTG
TGGGTGGTGCACAAATTCAACATTTTTACAGGAAGGAATGCCTACTTCTGCACGATGTGATGATTTAGAAGCCTTAAAAAAGAAGG
GTTGCCCTCCAGATGACATAGAAAATCCCAGAGGCTCCAAAGATATAAAGAAAAATAAAAATGTAACCAACCGTAGCAAAGGAACA
GCAGAGAAGCTCAAGCCAGAGGATATTACTCAGATCCAACCACAGCAGTTGGTTTTGCGATTAAGATCAGGGGAGCCACAGACA
TTTACATTAAAATTCAAGAGAGCTGAAGACTATCCCATTGACCTCTACTACCTTATGGACCTGTCTTACTCAATGAAAGACGATTTG
GAGAATGTAAAAAGTCTTGGAACAGATCTGATGAATGAAATGAGGAGGATTACTTCGGACTTCAGAATTGGATTTGGCTCATTTGT
GGAAAAGACTGTGATGCCTTACATTAGCACAACACCAGCTAAGCTCAGGAACCCTTGCACAAGTGAACAGAACTGCACCAGCCC
ATTTAGCTACAAAAATGTGCTCAGTCTTACTAATAAAGGAGAAGTATTTAATGAACTTGTTGGAAAACAGCGCATATCTGGAAATTTG
GATTCTCCAGAAGGTGGTTTCGATGCCATCATGCAAGTTGCAGTTTGTGGATCACTGATTGGCTGGAGGAATGTTACACGGCTGC
TGGTGTTTTCCACAGATGCCGGGTTTCACTTTGCTGGAGATGGGAAACTTGGTGGCATTGTTTTACCAAATGATGGACAATGTCA
CCTGGAAAATAATATGTACACAATGAGCCATTATTATGATTATCCTTCTATTGCTCACCTTGTCCAGAAACTGAGTGAAAATAATATT
CAGACAATTTTTGCAGTTACTGAAGAATTTCAGCCTGTTTACAAGGAGCTGAAAAACTTGATCCCTAAGTCAGCAGTAGGAACATTA
TCTGCAAATTCTAGCAATGTAATTCAGTTGATCATTGATGCATACAATTCCCTTTCCTCAGAAGTCATTTTGGAAAACGGCAAATTGT
CAGAAGGAGTAACAATAAGTTACAAATCTTACTGCAAGAACGGGGTGAATGGAACAGGGGAAAATGGAAGAAAATGTTCCAATATT
TCCATTGGAGATGAGGTTCAATTTGAAATTAGCATAACTTCAAATAAGTGTCCAAAAAAGGATTCTGACAGCTTTAAAATTAGGCCT
CTGGGCTTTACGGAGGAAGTAGAGGTTATTCTTCAGTACATCTGTGAATGTGAATGCCAAAGCGAAGGCATCCCTGAAAGTCCCA
AGTGTCATGAAGGAAATGGGACATTTGAGTGTGGCGCGTGCAGGTGCAATGAAGGGCGTGTTGGTAGACATTGTGAATGCAGCA
CAGATGAAGTTAACAGTGAAGACATGGATGCTTACTGCAGGAAAGAAAACAGTTCAGAAATCTGCAGTAACAATGGAGAGTGCGT
CTGCGGACAGTGTGTTTGTAGGAAGAGGGATAATACAAATGAAATTTATTCTGGCAAATTCTGCGAGTGTGATAATTTCAACTGTG
ATAGATCCAATGGCTTAATTTGTGGAGGAAATGGTGTTTGCAAGTGTCGTGTGTGTGAGTGCAACCCCAACTACACTGGCAGTGC
ATGTGACTGTTCTTTGGATACTAGTACTTGTGAAGCCAGCAACGGACAGATCTGCAATGGCCGGGGCATCTGCGAGTGTGGTGT
CTGTAAGTGTACAGATCCGAAGTTTCAAGGGCAAACGTGTGAGATGTGTCAGACCTGCCTTGGTGTCTGTGCTGAGCATAAAGA
ATGTGTTCAGTGCAGAGCCTTCAATAAAGGAGAAAAGAAAGACACATGCACACAGGAATGTTCCTATTTTAACATTACCAAGGTAG
AAAGTCGGGACAAATTACCCCAGCCGGTCCAACCTGATCCTGTGTCCCATTGTAAGGAGAAGGATGTTGACGACTGTTGGTTCTA
TTTTACGTATTCAGTGAATGGGAACAACGAGGTCATGGTTCATGTTGTGGAGAATCCAGAGTGTCCCACTGGTCCAGACATCATTC
CAATTGTAGCTGGTGTGGTTGCTGGAATTGTTCTTATTGGCCTTGCATTACTGCTGATATGGAAGCTTTTAATGATAATTCATGACA
GAAGGGAGTTTGCTAAATTTGAAAAGGAGAAAATGAATGCCAAATGGGACACGGGTGAAAATCCTATTTATAAGAGTGCCGTAACA
ACTGTGGTCAATCCGAAGTATGAGGGAAAATGA

YME1L1 CRISPR-I

Using EF1a-dCas9-KRAB-Blast dCas9 vector and sgRNA lentiviral vectors generously provided by Dr. Michael T McManus and Broad institute GPP sgRNA Design identified sgRNAs targeting YME1L1 (1: 5′-TTCCGTTTCTGGGAGGAGTG, 2: 5′-GCAGTAGCTG TAGGAAGGGG, and 3:CTCCTCCCAGAAACGGAAAA-5′) stable cell lines were generated *via* sequential selection of blasticidin (CRISPR-I) and puromycin (sgRNA), kill curve and qPCR validated.

IN VITRO RESPIROMETRY

Mitochondrial stress tests were performed with a Sea horse XF24e cellular respirometer on non-permeablized cells at ~ 96% confluence (100-k cells/well) in V7 microplates, with XF assay medium supplemented with 1 mM pyruvate (Gibco), 2 mM glutamine (Gibco),and 5 or 25-mM glucose (Sigma) at pH 7.4 and sequential additions via injection ports of oligomycin [1-μM final], FCCP [1-μM final], and antimycin A/rotenone [1-μM final] during respirometry (concentrated stock solutions solubilized in 100% ethanol [2.5 mM] for mitochondrial stress test compounds). OCR values presented with non-mitochondrial oxygen consumption deducted.

Atomic force microscopy

Knockdown of HSF1

pLKO.1 puro (Addgene #8453) was modified to carry:

Scr insert:

5'-CAACAAGATGAAGAGCACCAACTCGAGTTGGTGCTCTTCATCTTGTTGTTTTT, shRNA HSF1-1 TRCN0000007481 (HSF1):

5'-CCGGGCAGGTTGTTCATAGTCAGAACTCGAGTTCTGACTATGAACAACCTGCTTTTT, shRNA HSF1-2 TRCN0000318652 (HSF1):

5'-CCGGGCACATTCCATGCCCAAGTATCTCGAGATACTTGGGCATGGAATGTGCTTTTT

Constitutively active HSF1

CD510B-1_pCDH-CMV-MCS-EF1-Puro (SystemBio) vector was modified to carry the hHSF1ΔRD (Δ221–315) transgene (Nakai et al., 2000) under the CMV promoter.

ATGGATCTGCCCGTGGGCCCCGGCGCGGCGGGGCCCAGCAACGTCCCGGCCTTCCTGACCAAGCTGTGGACCCTCGTGAG
CGACCCGGACACCGACGCGCTCATCTGCTGGAGCCCGAGCGGGAACAGCTTCCACGTGTTCGACCAGGGCCAGTTTGCCAAG
GAGGTGCTGCCCAAGTACTTCAAGCACAACAACATGGCCAGCTTCGTGCGGCAGCTCAACATGTATGGCTTCCGGAAAGTGGTC

Please cite this article in press as: Tharp et al., Adhesion-mediated mechanosignaling forces mitohormesis, Cell Metabolism (2021), https://doi.org/10.1016/j.cmet.2021.04.017

CACATCGAGCAGGGCGGCCTGGTCAAGCCAGAGAGAGACGACACGGAGTTCCAGCACCCATGCTTCCTGCGTGGCCAGGAGC
AGCTCCTTGAGAACATCAAGAGGAAAGTGACCAGTGTGTCCACCCTGAAGAGTGAAGACATAAAGATCCGCCAGGACAGCGTCA
CCAAGCTGCTGACGGACGTGCAGCTGATGAAGGGGAAGCAGGAGTGCATGGACTCCAAGCTCCTGGCCATGAAGCATGAGAAT
GAGGCTCTGTGGCGGGAGGTGGCCAGCCTTCGGCAGAAGCATGCCCAGCAACAGAAAGTCGTCAACAAGCTCATTCAGTTCCTG
ATCTCACTGGTGCAGTCAAACCGGATCCTGGGGGTGAAGAGAAAGATCCCCCTGATGCTGAACGACAGTGGCTCAGCACATGGG
CGCCCATCTTCCGTGGACACCCTCTTGTCCCCGACCGCCCTCATTGACTCCATCCTGCGGGAGAGTGAACCTGCCCCCGCCTCC
GTCACAGCCCTCACGGACGCCAGGGGCCACACGGACACCGAGGGCCGGCCTCCCTCCCCCCCGCCCACCTCCACCCCTGAAA
AGTGCCTCAGCGTAGCCTGCCTGGACAAGAATGAGCTCAGTGACCACTTGGATGCTATGGACTCCAACGAGGATAACCTGCAGA
CCATGCTGAGCAGCCACGGCTTCAGCGTGGACACCAGTGCCCTGCTGGACCTGTTCAGCCCCTCGGTGACCGTGCCCGACATG
AGCCTGCCTGACCTTGACAGCAGCCTGGCCAGTATCCAAGAGCTCCTGTCTCCCCAGGAGCCCCCCAGGCCTCCCGAGGCAGA
GAACAGCAGCCCGGATTCAGGGAAGCAGCTGGTGCACTACACAGCGCAGCCGCTGTTCCTGCTGGACCCCGGCTCCGTGGACA
CCGGGAGCAACGACCTGCCGGTGCTGTTTGAGCTGGGAGAGGGCTCCTACTTCTCCGAAGGGGACGGCTTCGCCGAGGACCC
CACCATCTCCCTGCTGACAGGCTCGGAGCCTCCCAAAGCCAAGGACCCCACTGTCTCCTAG

SLC9A1 KO

MCF10A cells were transfected via PEI (https://www.addgene.org/protocols/transfection/) with pSpCas9(BB)-2A-GFP (PX458) - (Addgene #48138) carrying sgRNA for hSLC9A1 5'-GTTTGCCAACTACGAACACG (SLC9A1:HGLibA_45399) and H^+-suicide selected (Pouysségur et al., 1984) four separate times to isolate SCL9A1 KOs. ~15% of the cells survived the first H^+-suicide selection, ~90% survived the subsequent 4 sections.

C. elegans compound microscopy of mitochondria

Transgenic animals carrying vha-6p::MLS::mRuby (MLS was derived from atp-1: ATGTTGTCCAAACGCATTGTTACCGCTCTTAACA CCGCCGTCAAGGTCCAAAATGCCGGAATCGCCACCACCGCCCGCGGA) were grown from L1 to desired stage of adulthood on standard RNAi plates as described above. Animals were aged by hand-picking adults away from progeny using a pick daily until desired stage of adulthood. For imaging, adult worms are mounted on a glass slide in M9 solution, covered with a cover slip, and imaged immediately for a maximum of 10 minutes per slide. Animals were imaged on a Zeiss AxioObserver 7 LSM900 Airyscan 2 equipped with a 63x/1.4 Plan Aprochromat objective, MA-PMT detector, diode lasers (488 nm, 10mW, laser class 3B; 561 nm, 10 mW, laser class 4B), driven by ZenBlack software. Images were processed using ZEN Module Airyscan for 3D using default software settings. Images were analyzed using MitoMAPR (Zhang et al., 2019) across max projections keeping all parameters constant.

C. elegans Paraquat survival assay

Animals were grown to day 1 adulthood on standard RNAi plates as described above. 10 animals were picked into 75 μL of 100 mM paraquat solution prepared in M9 in a flat-bottom 96-well plate. >8 wells are used per condition for a minimum of 80 animals per replicate. Animals were scored every 2 hours for death. Plates are tapped gently, and any trashing or bending movement is scored as alive. Paraquat survival assays are performed with the experimenter blinded to the strain conditions during scoring and are repeated a minimum of 3 replicates per experiment.

C. elegans stereomicroscopy for fluorescent transcriptional reporters

Transgenic animals carrying *gst-4p::GFP* were grown on standard RNAi plates as described above until the L4 stage. L4 animals were washed off of plates using M9, centrifuged to pellet, and M9 was replaced with 50 mM paraquat prepared in M9. Animals were incubated rotating in a 20 °C incubator for two hours, and subsequently washed 2x with M9 solution. Animals were then plated on OP50 plates and recovered for 2 hours at 20 °C. For imaging, worms were picked onto a standard NGM plate containing 5 μL of 100 mM sodium azide to paralyze worms. Paralyzed worms were lined up, and imaged immediately on a Leica M250FA automated fluorescent stereomicroscope equipped with a Hamamatsu ORCA-ER camera, standard GFP filter, and driven by LAS-X software.

C. elegans biosorter analysis

For large-scale quantification of fluorescent animals, a Union Biometrica complex object parameter analysis sorter (COPAS) was used (for full details, refer to Daniele et al., 2017). Briefly, to quantify signal of *gst-4p::GFP*, animals treated as described above were washed off plates using M9, and run through the COPAS biosort using a 488 nm light source. Integrated fluorescence intensity normalized to the time of flight is collected automatically on the COPAS software, and then normalized again to the extinction to correct for both worm length and worm thickness.

ROCK:ER

pBABEpuro3 ROCK:ER (Croft and Olson, 2006) was generously provided by Dr. Michael F. Olson, packaged into retroviral particles with phoenix cells, and used to generate stable MCF10A cells lines which were activated with 1 μg/mL 4-hydroxytamoxifen (Sigma).

COX4L MTS tagged roGFP was expressed under the CMV promoter in a puromycin lentiviral transfer vector generated by the Dillin Lab (Dr. Brant Webster).

AFM and analyses were performed using an MFP3D-BIO inverted optical atomic force microscope mounted on a Nikon TE2000-U inverted fluorescence microscope (Asylum Research). 100k cells were seeded onto fibronectin coated 15 mm^2 coverslips and

Please cite this article in press as: Tharp et al., Adhesion-mediated mechanosignaling forces mitohormesis, Cell Metabolism (2021), https://doi.org/10.1016/j.cmet.2021.04.017

cultured for 24 h. Coverslips were anchored with permanent adhesive dots (Scotch, 00051141908113) to a glass slide that was then magnet-anchored to the stage of the microscope. All samples were measured in media with contact mode using Novascan cantilevers (5 μm radius, Probe 58, k = 0.06 N per m), which were calibrated using the thermal tune method. 36 force measurements were collected over a 250 × 250 μm grid per sample. The resulting force data were converted to elastic modulus values using the Hertz Model program (tissue samples were assumed to be noncompressible, and a Poisson's ratio of 0.5 was used in the calculation of theYoung's elastic modulus values) in IgorPro v.6.22, supplied by Asylum Research

For JC-9 staining, day 1 adult animals were transferred to a plate containing JC-9-treated bacteria (OP50 bacteria were grown during mid-log phase for 4 hours in LB containing 50 μM JC-9 at 37 °C to incorporate JC-9 into bacteria; then bacteria were washed 2x with fresh LB to remove excess JC-9). Animals were grown on JC-9 bacteria for 2 hours at 20 °C to label. After labeling, worms were moved onto standard OP50 plates and grown for an additional 1 hour at 20 °C to remove excess JC-9 from the gut. Animals were then washed off plates and immediately run on a biosorter using a 488 and 561 nm light source. Worm profile data was collected, and run through an orientation and quantification algorithm, LAMPro (Daniele et al., 2017). Briefly, integrated fluorescence intensity is measured throughout the entire profile of the worm and normalized to extinction throughout the length of the worm. Total integrated fluorescence of the entire worm was also calculated by normalizing to the time of flight and integrated extinction of the entire worm. JC-9 fluorescence at 515 nm was used to determine mitochondrial quantity, and the ratio of the fluorescence of 585 nm / 515 nm was used to determine mitochondrial membrane potential.

Lifespan assay

Lifespan measurements were performed on solid NGM plates with RNAi bacteria. Worms were synchronized via bleaching/L1 arrested as described above. Adult animals were moved away from progeny by moving worms onto fresh RNAi plates every day until D7-10 when progeny were no longer visible. Animals were then scored every 1-2 days for death until all animals were scored. Animals with bagging vulval explosion, or other age-unrelated deaths were censored and removed from quantification.

Lattice light sheet microscopy

We used a Custom build lattice light sheet microscope (Chen et al., 2014) to image MCF10A culture on polyacrylamide gels. Polyacrylamide gels (PA-gels) were formed on 5 mm round cover glass (Warner Instruments), coated with fibronectin and seeded with ~ 1000 cells per gel. The samples were cultured for 24 h in MCF10A media prior to imaging in DMEM (5 mM glucose) without phenol red supplemented with 5% Fetal Bovine serum. Samples were illuminated by 561 nm diode laser (0.5W Coherent) or 639 nm diode laser (1W Coherent) using an excitation objective (Special Optics, 0.65 NA with a working distance of 3.74-mm) at 2% AOTF transmittance and output laser power of 100 mW. The measured powers at the back focal plane of the illumination objective were in the range of 0.15-0.2 mW. Order transfer functions were calculated by acquiring Point-spread functions using 200-nm TetraSpeck beads adhered freshly to 5-mm glass coverslips (Invitrogen T7280) for each excitation wavelength and each acquisition filter set. The LLSM was realigned before each experiment.

For illumination we displayed on the spatial light modulator (SLM) a Square lattice generated by an interference pattern of 59 bessels beams separated by 1.67 um and cropped to 0.22 with a 0.325 inner NA and 0.40 outer NA, or by a an interference pattern of 83 bessels beams separated by 1.23 um and cropped to 0.22 with a 0.44 inner NA and 0.55 outer NA The lattice light sheet was dithered 15-25 um to obtain an homogenous illumination with 5% of flyback time. Fluorescent signal was collected by a Nikon detection objective (CFI Apo LWD 25XW, 1.1 NA, 2-mm working distance (WD)), coupled with a 500 mm focal length tube lens (Thorlabs), a set of Semrock filters (BL02-561R-25, BLP01-647R-25, and NF03-405-488-561-635E-25), and a sCMOS camera (Hamamatsu Orca Flash 4.0 v2) with a 103 nm/pixel magnification.

Z-Stacks (Volumes) were acquired by moving the Z-piezo in scanning mode while leaving the lattice light sheet static. The slices of the stacks were taken with an interval of 100-235 nm (S-axis) through ranges of 30-35 um at 20-100 ms exposuretime with 0 - 60 seconds intervals between volumes.

Raw data was flash corrected (Liu et al., 2017) and deconvolved using an iterative Richardson-Lucy algorithm (Chen et al., 2014) on two graphics processing units (GPU) (Nvidia, GeForce GTX Titan 4-Gb RAM). Flash calibration, flash correction, channel registration, Order transfer function calculation and Image deconvolution were done using the LLSpy open software (Lambert, 2019). Visualization of the images and volume inspection were done using Spimagine (https://github.com/maweigert/spimagine) and Clear volume (Royer et al., 2015).

For the glucose shock experiment, MCF10A cells were first localized under the LLSM. During the first 30 seconds of the acquisition, the glucose concentration was raised to a final concentration of 25 mM. The glucose infusion caused misalignment of the lattice light sheet microscope which was corrected manually during the first acquisition volume.

Fractal dimension and lacunarity

Due to the complex morphology of mitochondria networks, we chose to calculate the fractal dimension and lacunarity to describe its morphology. This analysis has been proven useful to characterize mitochondrial morphology in malignant mesothelioma (Lennon et al., 2016). For the analysis regions of 276x276 pixels containing mitochondrial network were sampled randomly from 4 representative microscopy images for each experimental condition. Regions with more than 25% of its area contained nucleus were excluded from the analysis. Each data point in Figure S1**E**, represent a sampled region. Each region was first low pass filtered with a radius of 8 pixels and a weight of 0.8 to enhance the mitochondria network signal. After each region was thresholded using the Huang Algorithm.

Please cite this article in press as: Tharp et al., Adhesion-mediated mechanosignaling forces mitohormesis, Cell Metabolism (2021), https://doi.org/10.1016/j.cmet.2021.04.017

For each binary-masked region we used FracLac (http://rsb.info.nih.gov/ij/plugins/fraclac/FLHelp/Introduction.htm) to calculate the fractal dimension (Db) and the lacunarity (lambda). For each region we increased linearly the sampled box until a maximum size of 50% of the region area the Db is calculated as the the average of Db from the Box scans. The fractal dimension was calculated using a regression to the logarithmic values of pixels with value 1 versus logarithm of the box size.

RNAseq

Total RNA was isolated using Trizol (Invitrogen), and RNAseq libraries (2 biological replicates per condition comprised of a pool of 4 PA-gel cultures each) prepared using KAPA mRNA HyperPrep Kit (Roche) and IDT dual indexed sequencing adaptors. Multiplexed libraries were sequenced on an Illumina HiSeq4000, and reads were aligned to the human genome (hg19) using RNA STAR (Dobin et al., 2013). Aligned reads were counted using HOMER (Lin et al., 2010), and hierarchical clustering was performed using Cluster (Eisen et al., 1998) and visualized with Java TreeView. Gene Ontology analysis was performed using Metascape (Zhou et al., 2019).

Mitochondrial ETC proteomics timsTOF

1 million cells were seeded on 50 mM^2 varied stiffness ECM coated PA-gels cultured for 24 h. Cells were washed with sterile PBS once, then cells were detached with cold PBS and a cell scraper (rubber policeman). Cell pellets were then suspended in 100 μL urea lysis buffer (ULB: 8M urea, 100 mM Tris, and 75 mM NaCl at pH 8). Probe sonicated 5 times for 2 s on ice. Protein concentrations were determined *via* BCA, and 100 μg of each sample was alkylated and reduced for 1 h at ~22 °C (protected from light) *via* the addition of a 10X concentrated stock (ARB: 400 mM 2-Chloroacetamide and 100 mM Tris(2-carboxyethyl)phosphine (TCEP) dissolved in ULB) yielding a final concentration of 40 mM 2-Chloroacetamide and 10 mM TCEP. Samples were then diluted, with a Tris/NaCl buffer (100 mM Tris and 75 mM NaCl at pH 8) containing 1 μg LysC (Promega, Va11A) per sample, to yield a final concertation of 2M urea during a 4 h digestion at ~22 °C (protected from light). Following the LysC digestion, 2 μg of Trypsin (Pierce, 1862746) was added and allowed to react with the sample overnight at 37 °C. The samples were then acidified with Trifluoroacetic acid (TFA) [~1% final] to yield a sample pH of 2. Samples were then desalted on C18 tips (Nest Group), the eluant was lyophilized, and then resuspended in 4% formic acid, 3% acetonitrile at 200 fmol/μL concentration. For each MS analysis, 1 μL of sample was separated over a 25 cm column packed with 1.9 μm Reprosil C18 particles (Dr. Maisch HPLC GmbH) by a nanoElute HPLC (Bruker). Separation was performed at 50 °C at a flow rate of 400 μL/min by the following gradient in 0.1% formic acid: 2% to 17% acetonitrile from 0 to 60 min, followed by 17% to 28% acetonitrile from 60 to 105 min. The eluant was directed electrospray ionized into a Bruker timsTOF Pro mass spectrometer and data was collected using data-dependent PASEF acquisition (Meier et al., 2018). Database searching and extraction of MS1 peptide abundances was performed using the MaxQuant algorithm (Cox and Mann, 2008), and all peptide and protein identifications were filtered to a 1% false-discovery rate. Searches were performed against a protein database of the human proteome (downloaded from Uniprot on 3/21/2018). Lastly quality control analysis was performed via artMS (http://artms.org) and statistical testing was performed with MSstats (Choi et al., 2014).

LC-MS/MS deuterium incorporation proteomics

1 million cells were seeded on 50 mM^2 varied stiffness PA-gels cultured for 24 h in 6% D_2O culture media in a 5% CO_2 incubator humidified with 5% D_2O. D_2O labeled cells were detached with cold PBS and a cell scraper (rubber policeman), pelleted with centrifugation, and mitochondrial fractions were isolated with the Mitochondria Isolation Kit for Cultured Cells (Thermo, 89874). Protein was isolated by flash freezing and sonication in PBS with 1 mM PMSF, 5 mM EDTA, and 1x Halt protease inhibitor (Thermo, 78440). Protein content was quantified via BCA (Pierce, 23225) and 100 μg of protein from each sample was trypsin (Pierce, 90057) digested overnight after reduction and alkylation with DTT, TFE, and iodoactamide (Russell et al., 2001). Trypsin-digested peptides were analyzed on a 6550 quadropole time of flight (Q-ToF) mass spectrometer equipped with Chip Cube nano ESI source (Agilent Technologies). High performance liquid chromatography (HPLC) separated the peptides using capillary and nano binary flow. Mobile phases were 95% acetonitrile/0.1% formic acid in LC-MS grade water. Peptides were eluted at 350 nL/minute flow rate with an 18 minute LC gradient. Each sample was analyzed once for protein/peptide identification in data-dependent MS/MS mode and once for peptide isotope analysis in MS mode. Acquired MS/MS spectra were extracted and searched using Spectrum Mill Proteomics Workbench software (Agilent Technologies) and a human protein database (https://www.uniprot.org/). Search results were validated with a global false discovery rate of 1%. A filtered list of peptides was collapsed into a nonredundant peptide formula database containing peptide elemental composition, mass, and retention time. This was used to extract mass isotope abundances (M0-M3) of each peptide from MS-only acquisition files with Mass Hunter Qualitative Analysis software (Agilent Technologies). Mass isotopomer distribution analysis (MIDA) was used to calculate peptide elemental composition and curve-fit parameters for predicting peptide isotope enrichment based on precursor body water enrichment (p) and the number (n) of amino acid C-H positions per peptide actively incorporating hydrogen (H) and deuterium (D) from body water. Subsequent data handling was performed using python-based scripts, with input of precursor body water enrichment for each subject, to yield fractional synthesis rate (FSR) data at the protein level. FSR data were filtered to exclude protein measurements with fewer than 2 peptide isotope measurements per protein.

Please cite this article in press as: Tharp et al., Adhesion-mediated mechanosignaling forces mitohormesis, Cell Metabolism (2021), https://doi.org/10.1016/j.cmet.2021.04.017

LC-MS metabolomics

1 million cells were seeded on 50 mm^2 varied stiffness ECM coated PA-gels cultured for 24 h. Cells were dissolved in 100% methanol doped with N-Ethylmaleimide (NEM) [8 mM,1 mg/mL] (Sigma-Aldrich, E1271) (Giustarini et al., 2013). Protein concentrations of the methanol extract was determined via BCA (Pierce, 23225) (5 uL transferred into 45 uL RIPA buffer, 5 uL of the RIPA dissolved solution assayed). Data was normalized to 100 μg per sample and polar metabolites were extracted in a total volume of 275 μl of 40:40:20 (acetonitrile:methanol:water) with inclusion of internal standard d_3N^{15}-serine (Cambridge Isotope Laboratories, #DNLM-6863). Extracted samples were centrifuged at 10,000 x g for 10 min and an aliquot of the supernatant was injected onto LC/MS where metabolites were separated by liquid chromatography. Analysis was performed with an electrospray ionization (ESI) source on an Agilent 6430 QQQ LC-MS/MS (Agilent Technologies). The capillary voltage was set to 3.0 kV, and the fragmentor voltage was set to 100 V, the drying gas temperature was 350 °C, the drying gas flow rate was 10 L/min, and the nebulizer pressure was 35 PSI. Polar metabolites were identified by SRM of the transition from precursor to product ions at associated optimized collision energies and retention times (Louie et al., 2016). Quantification of metabolites was performed by integrating the area under the curve and then normalizing to internal standard values. All metabolite levels are expressed as relative abundances compared to the control group.

^{13}C6-glucose LC-MS metabolomics

1 million cells were seeded on 50 mm^2 varied stiffness ECM coated PA-gels cultured for 22 h in 5 mM glucose DMEM based MCF10A media. The media was exchanged for media with 5 mM ^{13}C6-Glucose (Cambridge Isotope Laboratories, CLM-1396) DMEM based MCF10A media Cells for 2 h. Cells were washed twice with PBS and extracted with mass spectrometry grade 80% methanol (ThermoFisher, A456-1) and 20% water (ThermoFisher, W6500) supplemented with 5 nmol DL-Norvaline (Sigma, N7502). Protein concentrations of the methanol extract was determined via BCA (Pierce, 23225) with no significant variability assessed (5 uL transferred into 45 uL RIPA buffer, 5 uL of the RIPA dissolved solution assayed). Insoluble material was pelleted in a 4°C centrifuge at 16k x g, supernatant was transferred and dried in a Speedvac. Dried metabolites were resuspended in 50% ACN:water and 1/10th of the volume was loaded onto a Luna 3 um NH2 100A (150 × 2.0 mm) column (Phenomenex). The chromatographic separation was performed on a Vanquish Flex (Thermo Scientific) with mobile phases A (5 mM NH_4AcO pH 9.9) and B (ACN) and a flow rate of 200 μL/min. A linear gradient from 15% A to 95% A over 18 min was followed by 9 min isocratic flow at 95% A and reequilibration to 15% A. Metabolites were detected with a Thermo Scientific Q Exactive mass spectrometer run with polarity switching (+3.5 kV / -3.5 kV) in full scan mode with an m/z range of 65-975. TraceFinder 4.1 (Thermo Scientific) was used to quantify the targeted metabolites by area under the curve using expected retention time and accurate mass measurements (< 5 ppm). Values were normalized to cell number and sample protein concentration. Relative amounts of metabolites were calculated by summing up the values for all isotopologues of a given metabolite. Fractional contributional (FC) of ^{13}C carbons to total carbon for each metabolite was calculated. Data analysis was accomplished using in-house developed R scripts.

Paraquat survival

10 mM paraquat (Acros Organics, 227320010) was dissolved into media and added to cell culture vessels and allowed to affect the cells for 24 h, experiments were always performed with a fresh suspension of paraquat. After 24 h of paraquat treatment cells were fixed with 4% PFA and stained for cleaved caspase 3 (Cell Signaling, 9661).

QUANTIFICATION AND STATISTICAL ANALYSIS

Data displayed represent at least three independent experiments, unless otherwise specified. Figure legends contain biological and technical replicate information. Plots include each data point, mean, and SEM. Student's t test with 95% confidence interval was used to determine differences between two comparable groups. ANOVA with 95% confidence interval was used to compare three or more comparable groups. Grubb's test was used to detect distributions for outliers. Statistical comparisons were completed Graphpad Prism 6 software:

Figure 1. Data shown represents ± SEM. *P < 0.05, **P < 0.01, ***P < 0.005, < 0.0001 via two-tailed unpaired Student t test.

Figure 2. Data shown represents ± SEM. *P < 0.05, **P < 0.01, ***P < 0.005, < 0.0001 via one-way ANOVA with Tukey test for multiple comparisons to 400 Pa 5 mM Glucose (B and C) or 25 mM glucose (D).

Figure 3. Data shown represents ± SEM. *P < 0.05, **P < 0.01, ***P < 0.005, < 0.0001 via two-tailed unpaired Student t test in (D) and one-way ANOVA with Tukey test for multiple comparisons in (B and C).

Figure 4. Data shown represents ± SEM. *P < 0.05, **P < 0.01, ***P < 0.005, < 0.0001 via one-way ANOVA with Tukey test for multiple comparisons in (E, G, J and K).

Figure 6. Data shown represents ± SEM. *P < 0.05, **P < 0.01, ***P < 0.005, < 0.0001 via two-tailed unpaired Student t test in (D, F, and I) and one-way ANOVA with Tukey test for multiple comparisons in (C, G, and H).

Figure 7. Data shown represents ± SEM. *P < 0.05, **P < 0.01, ***P < 0.005, < 0.0001 via one-way ANOVA with Tukey test for multiple comparisons in (B and F).

Figure S1. Data shown represent ± SEM. *P < 0.05, **P < 0.01, ***P < 0.005, < 0.0001 via two-tailed unpaired Student t test.

Figure S2. Data shown represent ± SEM. *P < 0.05, **P < 0.01, ***P < 0.005, < 0.0001 via two-tailed unpaired Student t test (G-H), one-way ANOVA with Tukey test for multiple comparisons (B, and D-E), or Mann-Whitney (I-L).

Figure S3. Data shown represent ± SEM. *P < 0.05, **P < 0.01, ***P < 0.005, < 0.0001 via two-tailed unpaired Student t test (A-E, G, H, K, and M) or one-way ANOVA with Tukey test for multiple comparisons (I and L).

Figure S4. Data shown represent ± SEM. *P < 0.05, **P < 0.01, ***P < 0.005, < 0.0001 via two-tailed unpaired Student t test (E) or one-way ANOVA with Tukey test for multiple comparisons (B).

Figure S6. Data shown represent ± SEM. *P < 0.05, **P < 0.01, ***P < 0.005, < 0.0001 via two-tailed unpaired Student t test (C, E, and I) or one-way ANOVA with Tukey test for multiple comparisons (B and F-H).

Figure S7. Data shown represent ± SEM. *P < 0.05, **P < 0.01, ***P < 0.005, < 0.0001 via one-way ANOVA with Tukey test for multiple comparisons (A-B, E, and H).